Article

A Data-Driven Study of the Drivers of Stratospheric Circulation via Reduced Order Modeling and Data Assimilation

Julie Sherman [1,*], Christian Sampson [2], Emmanuel Fleurantin [3], Zhimin Wu [4] and Christopher K. R. T. Jones [3]

1 Department of Mathematics, University of Utah, Salt Lake City, UT 84112, USA
2 Joint Center for Satellite Data Assimilation, Boulder, CO 80301, USA; christian.sampson@gmail.com
3 Department of Mathematics, George Mason University, Fairfax, VA 22030, USA; efleuran@gmu.edu (E.F.); ckrtj@renci.org (C.K.R.T.J.)
4 School of Mathematical and Statistical Sciences, Arizona State University, Tempe, AZ 85287, USA; zhiminwu@asu.edu
* Correspondence: sherman@math.utah.edu

Abstract: Stratospheric dynamics are strongly affected by the absorption/emission of radiation in the Earth's atmosphere and Rossby waves that propagate upward from the troposphere, perturbing the zonal flow. Reduced order models of stratospheric wave–zonal interactions, which parameterize these effects, have been used to study interannual variability in stratospheric zonal winds and sudden stratospheric warming (SSW) events. These models are most sensitive to two main parameters: Λ, forcing the mean radiative zonal wind gradient, and h, a perturbation parameter representing the effect of Rossby waves. We take one such reduced order model with 20 years of ECMWF atmospheric reanalysis data and estimate Λ and h using both a particle filter and an ensemble smoother to investigate if the highly-simplified model can accurately reproduce the averaged reanalysis data and which parameter properties may be required to do so. We find that by allowing additional complexity via an unparameterized $\Lambda(t)$, the model output can closely match the reanalysis data while maintaining behavior consistent with the dynamical properties of the reduced-order model. Furthermore, our analysis shows physical signatures in the parameter estimates around known SSW events. This work provides a data-driven examination of these important parameters representing fundamental stratospheric processes through the lens and tractability of a reduced order model, shown to be physically representative of the relevant atmospheric dynamics.

Keywords: particle filter; ensemble smoother; sudden stratospheric warming; bistability; reanalysis data; dynamical systems; synoptic-scale meteorology

1. Introduction

1.1. General Background

Stratospheric polar circulation in the northern hemisphere, often referred to as the polar vortex, is a counterclockwise cyclonic circulation resulting from the strong temperature difference between the polar and subtropical regions that forms during the autumn and winter as solar radiation in the Arctic diminishes. This cyclonic circulation extends from the surface to the upper part of the stratosphere, often referred to separately as the tropospheric (near the surface) and stratospheric (near the top of the stratosphere) polar vortex. Changes in the stratospheric polar vortex can have strong effects on the tropospheric vortex and thus it plays a significant role in winter weather conditions in the northern hemisphere.

For decades, models of stratospheric circulation have sought to explain and predict variability in wintertime polar vortex dynamics via mechanistic and/or phenomenological processes [1–5]. A well-studied method of stratospheric modeling uses a quasi-geostrophic β-plane channel model to study wave–mean zonal flow interactions. An early model of this type by Holton and Mass [6] and its many extensions depend highly on two fundamental processes:

1. The interaction with waves propagating up from the troposphere;
2. Differential radiative heating.

Furthermore, such models have shown to exhibit mathematical properties consistent with atmospheric realizations including multiple stable or metastable equilibria associated with atmospheric blocking in the presence of external forcing

The two physical factors above are known to radically influence the polar vortex and are included as important control parameters in these models. First, the weakening of the polar vortex can be caused by large amplitude Rossby waves, also known as planetary waves, which propagate upward from the ground and interfere with the zonal wind in the stratosphere. Rossby waves are caused by topography as well as land–sea contrasts and can be hard to measure directly. Another factor that influences the polar vortex is the vertical gradient of radiative zonal wind. This is associated with solar forcing and is largest when there is high differential heating. Indeed, it is the changes in the differential heating throughout the seasons that lead to the annual formation and breakdown of the polar vortex in the fall and spring, respectively.

A sudden stratospheric warming (SSW) event can also lead to a breakdown in the polar vortex, which can cause severe weather at lower latitudes. An SSW event can be generically categorized by a rapid warming of the stratosphere near the pole, which leads to a decrease in differential heating weakening and even collapsing the cyclonic circulation of the polar vortex. Two theories have been proposed to explain the occurrence of SSWs that correspond with the control parameters of the reduced order models. First, enhanced planetary waves are known to transfer momentum and heat from the troposphere to the stratosphere, which alters the large-scale circulation [7,8]. Alternatively, it is understood that the vertical shear in the stratosphere is key to controlling upward propagation of waves through the lower boundary. Therefore, for smaller latitudinal temperature gradients, waves are more disruptive to zonal stratospheric flow [8,9].

Reconstructions of global weather patterns are routinely done by marrying available historical data to large-scale global circulation models through data assimilation (DA). Having a time record of global observations is key for advancement, however, they are irregular in space, time, and quality. By combining data and model, a complete picture of a global weather pattern time series can be formed. An example of such a reanalysis can be found through the European Center for Medium-Range Weather Forecasts (ECMWF) [10]. These datasets can aid scientists working to understand geophysical processes and changing climate conditions and develop new tools to improve predictions.

While large reanalysis datasets provide a plethora of information about the Earth system, they are extremely complex and lack the tractability of reduced order models. These models highlight the most important physical processes at play and can provide strong conceptual understanding, often leading to new ideas. By considering only the most influential processes, one can build a simplified model of stratospheric dynamics that maintains a mechanistic understanding of the system while ignoring or averaging components less relevant to large-scale and long-term behavior. In this work, we aim to leverage the complex information available in a large reanalysis dataset via DA to provide estimates and assess the dynamics of important, physically-based parameters in the context of a reduced order model.

1.2. Data Assimilation and Reduced-Order Models

Data assimilation has extremely useful applications in reduced order modeling. In particular, it can give a sense of suitability of the simplified model to the observed data as well as to estimate important parameters representing the physical characteristics. DA also allows for simultaneous estimation of model parameters via a number of methods (for an overview, see Ref. [11]). Assimilating reanalysis data with a reduced order model therefore provides a convenient way to assess the model and estimate the values and relevance of essential parameters controlling the system.

There are a great number of DA algorithms adapted to address a variety of situations. One of the most general is the particle filter, also known as the bootstrap filter. This is an ensemble-based, recursive algorithm that uses resampling and Bayes' Theorem to derive an empirical distribution that is asymptotically equivalent to the true distribution. This algorithm is more general than the better known Kalman filter as it does not assume linearity of the system nor normality of distributions [12].

We also explore the use of an Ensemble Smoother with Multiple Data Assimilation (ESMDA), updating the parameters that result in bias in the solution. This method allows for the estimation of time-dependent parameters since fitting their values at a given time can be adjusted to predict data at later times. Consequently, we are updating the parameters in the past to remove the bias in the solution before it happens. Some examples of iterative ensemble smoothers can be found in Refs. [13,14], in the geosciences in Ref. [15], or petroleum reservoir modeling in Ref. [16]. The simplicity of the chosen reduced order model makes this analysis possible as we are able to initialize large ensembles at a low computational cost. It also serves as a baseline in complexity with more detailed versions of the model available for further studies on higher order dynamics.

1.3. Our Main Focus

In this work, multiple data assimilation schemes were applied to a reduced order model of the polar vortex published by Ruzmaikin et al. in 2003 [17]. A highly reduced version of the original Holton and Mass model [6], this model is a nonlinear system of ordinary differential equations that exhibits bistability for certain parameter ranges [17]. Its dynamics are closely tied to parameters related to radiative forcing due to differential heating, Λ, and interactions with large-amplitude Rossby waves propagating upwards from the troposphere, h. The bistability of this model is relevant to meteorological phenomena including multiple stable states associated with atmospheric blocking events. This motivates the use of the particle filter, as we expect bimodal ensemble distributions. However, the particle filter ultimately fails to accurately describe the reanalysis data, so we turn to ESMDA, as it allows for added complexity through time-varying parameter estimations.

Through this work, we aim to assess the ability of this reduced order model to represent real world variability and, if it can, what it takes to do so. We find that when the controlling parameters are allowed to sufficiently vary in time, this reduced order model can produce mean zonal winds that closely match the reanalysis data. We also find that parameter regimes exist where the estimated parameters exhibit behavior that can be viewed as physically consistent with what one might expect during SSW events. We also comment on where we see the model possibly falling short. Thus, we are able to provide insights into patterns and trends in physically-based parameters using the simplicity of a reduced-order model while ensuring its applicability through assimilating reanalysis data.

1.4. Outline of the Paper

The paper is structured as follows. In Section 2 we discuss the materials and methods. We present the Ruzmaikin model in Section 2.1, the ECMWF data used in Section 2.2, and our data assimilation analysis methods in Section 2.3. In Section 3, we discuss our results: first using the particle filter in Section 3.1, then with ESMDA in Section 3.2. With the particle filter, we consider hyperparameter estimation and examine ECMWF data assimilation. With ESMDA, we deliberate on the parameters that we are estimating, the calibration of our runs with twin experiments, and different scenarios for estimating control parameters $\Lambda(t)$ and $h(t)$. Then, in Section 3.3 we explore our ESMDA analysis results in the context of historical atmospheric conditions, including around SSW events and trends over the 20-year period. Finally, Section 4 is dedicated to discussing our approach and concluding remarks.

2. Materials and Methods

2.1. Ruzmaikin Model

Considering the two driving forces highlighted above, Ruzmaikin et al., [17], developed a simple dynamical model composed of three ordinary differential equations (ODEs) that describe an atmospheric system localized as one point in the stratosphere. The "Ruzmaikin model" is a highly truncated version of the Holton and Mass 1976 model (the "HM76" model) of stratospheric wave-zonal flow interactions. It is obtained by considering only one longitudinal and one latitudinal mode of the HM76 model and fixing the vertical level to 25 km log-pressure height using finite differences. Details on the derivation of the model can be found in Appendix A. Although such a one-dimensional model cannot realistically describe the complicated stratospheric dynamics, it captures the essential mechanism of interactions between planetary waves, radiative forcing, and the zonal wind.

The Ruzmaikin model appears in the final form of three ODEs with state variables, X, Y, and U, where X and Y represent the real and imaginary parts of the streamfunction, respectively, and U represents mean zonal wind velocity. The system of ODE's is given by

$$\dot{X} = -X/\tau_1 - rY + sUY - \xi h + \delta_w \dot{h} \tag{1}$$

$$\dot{Y} = -Y/\tau_1 + rX - sUX + \zeta hU \tag{2}$$

$$\dot{U} = -(U - U_R)/\tau_2 - \eta hY - \delta_\Lambda \dot{\Lambda}. \tag{3}$$

Two control parameters are used in HM76 as well as the Ruzmaikin model, and all other parameters are fixed at their typical atmospheric values (Table A1). The first control parameter is the vertical gradient of the mean radiative zonal wind, $\Lambda(t) = dU_R/dz$, where it is assumed that $U_R(z,t) = U_R(0,t) + \Lambda(t)z$. In addition, using standard notations found in Ref. [18] in log-pressure coordinates, dU_R/dz is also related to the gradient of radiative equilibrium temperature $\bar{T}$ with respect to latitude y [19] through the relation,

$$f_0 \frac{dU_R}{dz} = -\frac{R}{H}\frac{d\bar{T}}{dy}. \tag{4}$$

In this case, $\Lambda(t)$ is a time-dependent parameter accounting for both the seasonal variability and the 11-year solar cycle variability of solar radiation. Specifically, Λ is assumed to take the form

$$\Lambda(t) = \Lambda_0 + \Lambda_a \sin\left(\frac{2\pi t}{1 \text{ year}}\right) + \epsilon\Lambda_0 \sin^2\left(\frac{\pi t}{11 \text{ year}}\right). \tag{5}$$

In Section 3.2 we will allow $\Lambda(t)$ to be far more dynamic and show that this is necessary for the model to capture the reanalysis data. This may imply that unresolved physics need to be included in this parameter for it to be more representative of reality.

The other control parameter characterizes the initial planetary wave amplitude and is denoted by h. Specifically, it is equivalent to the perturbation at the ground level, related to the wave streamfunction, Ψ, by $h(t) = \Psi(0,t)f_0/g$. While several works have explored various time or spatially-dependent parameterizations of h in similar models [6,20,21], Ruzmaikin et al. fixes h as constant. Sensitivity analysis confirms that the model is most sensitive to the two parameters h and Λ [22].

Further analysis of the influence of Λ and h (considered independently as constants) on equilibrium solutions show the existence of pitchfork bifurcations leading to bistability (Ref. [17], Figures 2 and 3). For instance, with relatively small values of h corresponding to low amplitude Rossby waves, there is a single equilibrium of relatively large mean zonal wind ($U_e \approx 35$ m/s). For very large values of h, corresponding to high amplitude Rossby waves, there is a single equilibrium of low mean zonal wind ($U_e \approx 21$ m/s). However, between these two extremes there is an area of bistability, for which both strong and weak polar vortices are achievable for the same value of h. Similarly, varying a constant Λ also

leads to a bifurcation of equilibrium values of zonal wind (Ref. [17], Figure 2). Note again the region of bistability for $\Lambda \gtrsim 0.75$ m/s/km when $h = 68$ m is fixed.

2.2. ECMWF Data

Twenty years (1999 to 2018) of zonal wind data were obtained from the European Center for Medium-Range Weather Forecasts (ECMWF) Reanalysis-Interim (or "ERA-Interim"), a global atmospheric reanalysis available from 1979. The reanalysis is based on a 2006 release of the ECWMF's Integrated Forecast System (IFS). The data assimilation system of ERA-Interim uses a 4-dimensional variational analysis (4D-Var) with a 12-h analysis window. More details of the ERA-Interim archive can be found in Ref. [23] and Ref. [24], Section 6.2.

The zonal wind of the Ruzmaikin model (variable U in Equations (1)–(3)) is equivalent to "U component of wind" provided by ECMWF Reanalysis-Interim archive. This data is available at the $1° \times 1°$ horizontal, 10 mb vertical (in the upper stratosphere), and four times daily resolution. Thus, we average according to the assumptions of the Ruzmaikin model: the vertical level is fixed at 25 km log-pressure height, and the latitudinal channel is centered at $60°$ N. First, daily mean zonal wind data is obtained by averaging over the four given wind data values per day. Thus, the processed dataset provides zonal wind "observations" as daily averages of the wind from 1 January 1999 to 31 December 2018. Next, daily averaged data from the pressure levels of 20 mb and 30 mb are interpolated to 25 km log-pressure height by linear approximation in the log-pressure vertical coordinate. Finally, as the Ruzmaikin model is confined to a latitudinal channel centered at $60°$ N with a meridional extent of $60°$ latitude, daily means of zonal wind interpolated to 25 km log-pressure height are then averaged over a latitudinal window centered at $60°$ N with a meridional extent of $20°$ latitude. Note that we also tested larger meridional window sizes, but these results are excluded, as the greater amount of averaging generally produced lower wind speeds and muted winter "peaks," as seen in Figure 1b.

We note that there is evidence of bistability in the ECMWF data, evidenced in Figure 1. Indeed, in Figure 1a, we see examples of two dates with representative behaviors of the polar vortex. On one hand, the jet may have high winds that are centered around the north pole. However, when the jet is destabilized, it rotates at lower speeds, and can be off-centered. These multiple winter states are also evident in the full-averaged data in Figure 1b. In particular with smaller meridional averaging windows, winter peak winds are either high (∼35–45 m/s) or low (∼20–30 m/s). Thus, it is our purpose to understand how the bistability of the reduced-order model relates to the bistability of the ERA-Interim data via data assimilation.
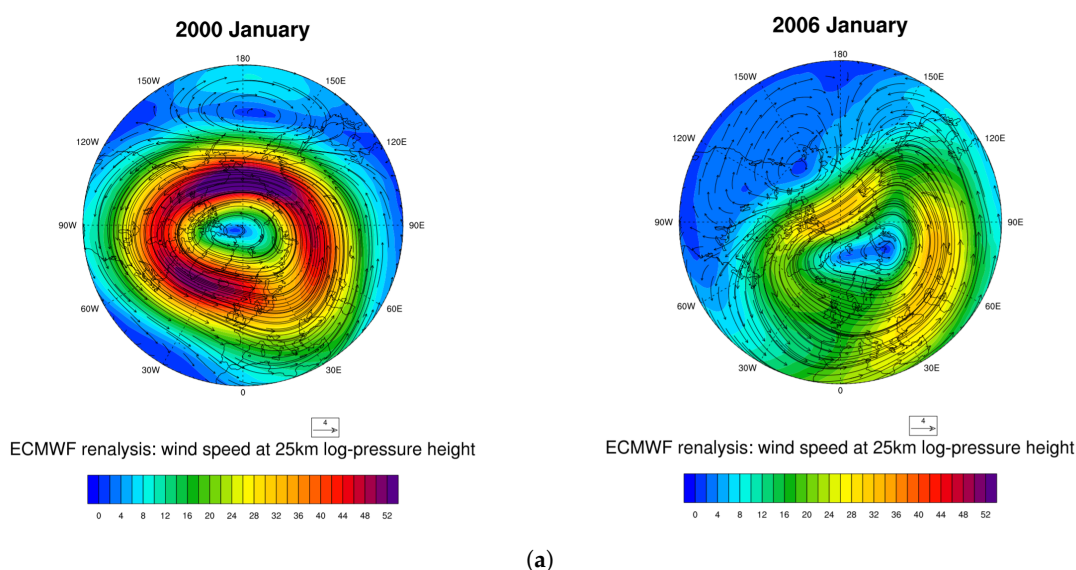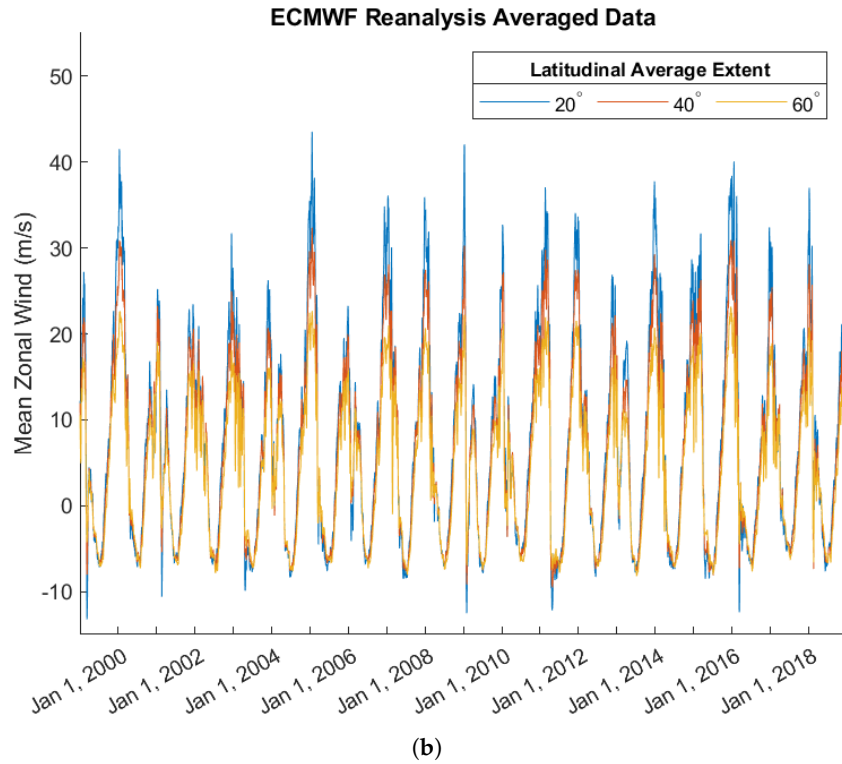

(a)

Figure 1. *Cont.*

(**b**)

Figure 1. Averaged ECMWF ERA−Interim data.

2.3. Data Assimilation

2.3.1. Particle Filter

The first DA method explored is the particle filter. This method is desirable because it allows for nonlinear dynamics and requires no distributional assumptions. In particular, due to the bistability of the system, we expect an ensemble of state variables to exhibit bimodality, thereby violating the normality assumption of the more common Kalman filter.

A detailed description of the mathematical and algorithmic framework behind the particle filter as well as its implementation in this context can be found in Appendix B. Essentially, the particle filter uses recursion and Bayes's rule (6) to approximate the distribution of the state vector at discrete time k, denoted x_k, given the set of all observations, y_i, up to and including time k,

$$p(x_k|y_1,\ldots,y_k) = \frac{p(y_k|x_k)p(x_k|y_1,\ldots,y_{k-1})}{p(y_k|y_1,\ldots,y_{k-1})}. \tag{6}$$

Lacking an analytical solution in the general case, one can instead use an iterative process of simulation and resampling to approximate the desired distribution. Indeed, each time an observation y_k, is obtained, if an ensemble (of size n_{ens}) of forecasted state vectors $\{x_k^*(i) : i = 1, \ldots, n_{\text{ens}}\}$ is resampled according to the normalized probabilities

$$q_i = \frac{p(y_k|x_k^*(i))}{\sum_{j=1}^{n_{\text{ens}}} p(y_k|x_k^*(j))}, \tag{7}$$

then the updated ensemble $\{x_k(i) : i = 1, \ldots, n_{\text{ens}}\}$ is distributed as $p(x_k|y_1, \ldots, y_k)$ [25].

Parameter estimation is easily realized by appending the state vector x_k of the dynamical model with the parameters of interest. In this case,

$$x_k = \begin{pmatrix} X & Y & U & h & \Lambda_0 & \Lambda_a \end{pmatrix}^T, \tag{8}$$

where Λ_0 and Λ_a are coefficients of the prescribed form for $\Lambda(t)$ in Equation (5). The observed variable, the mean zonal wind speed, is $y_k = U(k)$. Note that we also tested the particle filter with $x_k = \begin{pmatrix} X & Y & U & h \end{pmatrix}^T$, and $x_k = \begin{pmatrix} X & Y & U & \Lambda_0 & \Lambda_a \end{pmatrix}^T$, but generally the fits were inferior, and the results are omitted.

This algorithm was implemented in MATLAB via adaptations to a publicly available particle filter tutorial [26].

As it is also of interest how the bistability of the model manifests as bimodality within the particle filter, and the Sarle Bimodality Coefficient (BC) is computed for each experiment. The formula for the bimodality coefficient is given by

$$\text{BC} = \frac{m_3^2 + 1}{m_4 + 3 \cdot \frac{(n-1)^2}{(n-2)(n-3)}}, \tag{9}$$

where m_3 is the skewness of the sample, and m_4 is the excess kurtosis. BC is in the range of 0 (perfectly unimodal) to 1 (perfectly bimodal). The bimodality coefficient of a uniform distribution is $\text{BC}_{\text{Unif}} = 5/9$ and used as a benchmark, for values of BC above BC_{Unif} indicate bimodality of the distribution. It has been assessed in a number of studies and determined a good indicator of bimodality, although it can suffer from "false positives" particularly in the case of highly skewed distributions [27,28].

2.3.2. ESMDA

The next method of DA used in this paper is ESMDA. Ensemble smoother techniques can be derived by assuming a perfect forward model

$$y = g(x). \tag{10}$$

In general, x is a vector containing the realization of model parameters, and y consists of the uniquely predicted measurements. We want to find the set of model parameters x that produce the observed data.

Assume that the observations d are perturbed stochastically from the truth

$$d \leftarrow y + e, \tag{11}$$

where e represent errors from our model. This can be formulated as a Bayesian problem

$$f(x \mid d) \propto f(d \mid g(x)) f(x). \tag{12}$$

This defines the so-called smoothing problem. Our current approach is to use ensemble methods to approximately solve this equation. In order to do so, we seek to minimize the cost function below iteratively

$$J(x_j^{n+1}) = (x_j^{n+1} - x_j^n)^T (C_{xx}^n)^{-1} (x_j^{n+1} - x_j^n) + \left(g(x_j^{n+1}) - d - \sqrt{a^{n+1}e_j^n}\right)^T (a^{n+1}C_{dd})^{-1} \left(g(x_j^{n+1}) - d - \sqrt{a^{n+1}e_j^n}\right), \tag{13}$$

where

$$\sum_{n=1}^{N_{mda}} \frac{1}{a^n} = 1.$$

We proceed as follows: we initially sample parameters $x_{j,0} \sim N(x^f, C_{xx})$ and generate an ensemble of predicted observations $y_{j,0} = g(x_{j,0})$. We then use this ensemble to construct covariance matrices $\tilde{C}_{yy}^n$ and $\tilde{C}_{xy}^n$. We continue by perturbing observations, one for each member

$$d_j^n = d + e_j^n, \quad e_j^n \sim N(0, a^{n+1}C_{dd}). \tag{14}$$

We now update each member according to

$$x_j^{n+1} = x_j^n + \tilde{C}_{xy}^n \left(\tilde{C}_{yy}^n + a^{n+1} C_{dd} \right)^{-1} (d_j^n - y_j^n). \tag{15}$$

We finally forecast with the updated parameters using

$$y_j^{n+1} = g(x_j^{n+1}),$$

and repeat to $N_{mda} - 1$ steps. For simplicity, we summarize the ensemble methods used below

- We start by sampling a large ensemble of realizations of the prior uncertain parameters, given their prescribed first-guess values and standard deviations;
- We then integrate the ensemble of model realizations forward in time to produce a prior ensemble prediction, which also characterizes the uncertainty;
- We compute the posterior ensemble of parameters by making use of the misfit between prediction and observations, and the correlations between the input parameters and the predicted measurements;
- Ultimately, we compute the posterior ensemble prediction by a forward ensemble integration. The posterior ensemble is then the "optimal" model prediction with the ensemble spread representing the uncertainty.

More about ESMDA can be found in Ref. [29] and recent work using parameter estimation and ESMDA can be found in Ref. [30]. The code we used to preform the ESMDA analysis is modified from code developed by Dr. Geir Evensen to perform ESMDA analysis with a SEIR epedimic model [31].

2.3.3. Twin Model Analysis

This section describes the process through which the DA methods were tuned, assessed, and used to provide insights into key stratospheric circulation drivers. We determine appropriate values through twin model experiments in which data from a known "truth" is assimilated. This is an important first test of the data assimilation system that has been widely implemented over several decades and disciplines [28,32–34]. For the particle filter, twin model experiments were used to determine appropriate ranges for hyperparameters including assimilation period (number of days between observations and associated updates), observation error, and ensemble size. In the context of ESMDA identical twin experiments were used to assess the influence of decorrelation lengths.

First, identical twin model experiments were employed, using synthetic data from simulating the underlying model (Equations (1)–(3) with fixed $h = 68$ m, and Λ as in (5) with $\Lambda_0 = 0.75$ m/s/km and $\Lambda_a = 2.25$ m/s/km, and $\epsilon = 0.3$. Mean-zero Gaussian noise with variance σ_{obs}^2 was added to the variable U and then assimilated as the observed data. The data assimilation schemes were then applied with varying combinations of hyperparameters and statistics computed to compare the ensemble distribution to the known truth. We took the mean of the ensemble members as the assimilation analysis and compared it to the truth via the root mean squared error (RMSE)

$$\text{RMSE} = \sqrt{\frac{1}{N} \sum_{t=1}^{N} \left(\overline{U}_{\text{ens}}(t) - U_{\text{truth}}(t) \right)^2}. \tag{16}$$

Note that for the particle filter analysis, RMSE is computed on the dimensionalized values and only over the last 10 years of assimilation, thereby considering the first 10 years as a spin-up before the analysis. In a similar way we assessed the recovery of known parameters h, Λ_0, and Λ_a under various hyperparameters using RMSE.

Fraternal twin model experiments were used to assess the DA scheme's ability to recover data that comes from a model different than that being implemented in the algo-

rithm, under various hyperparameters. Here, the ERA-Interim reanalysis wind speed data is smoothed and considered the "truth" against which to compare the analysis mean of ensemble distribution. The RMSE is again calculated to measure goodness of fit.

3. Results

3.1. Particle Filter

3.1.1. Identical Twin Model Experiments

As described in Section 2.3.3, identical twin experiments were run on other hyperparameters including observation error, ensemble size, and assimilation period. Comparing RMSE for varying ensemble size, n_{ens}, shows a common pattern of decreasing until some critical size, after which increases in ensemble size no longer improve the estimation. Thus, it is sufficient and efficient to choose an ensemble size that is just larger than the value at which RMSE ceases to decrease. The ensemble size is fixed at $n_{\text{ens}} = 300$ for subsequent analyses.

Assimilation period refers to the length of time between consecutive observations of the system/updates of the ensemble. RMSE behaves intuitively for the fixed assimilation period and variable observation error and is demonstrated in (vertical slices of) Figure 2. Indeed, when the observations are very accurate (small σ_{obs}^2) the particle filter is more successful at estimating the truth (small RMSE). However, as the observation error increases, so does the measure of error of the ensemble average. Note that the observation error corresponds to the non-dimensionalized wind speed data, which has a maximum of 1.08.
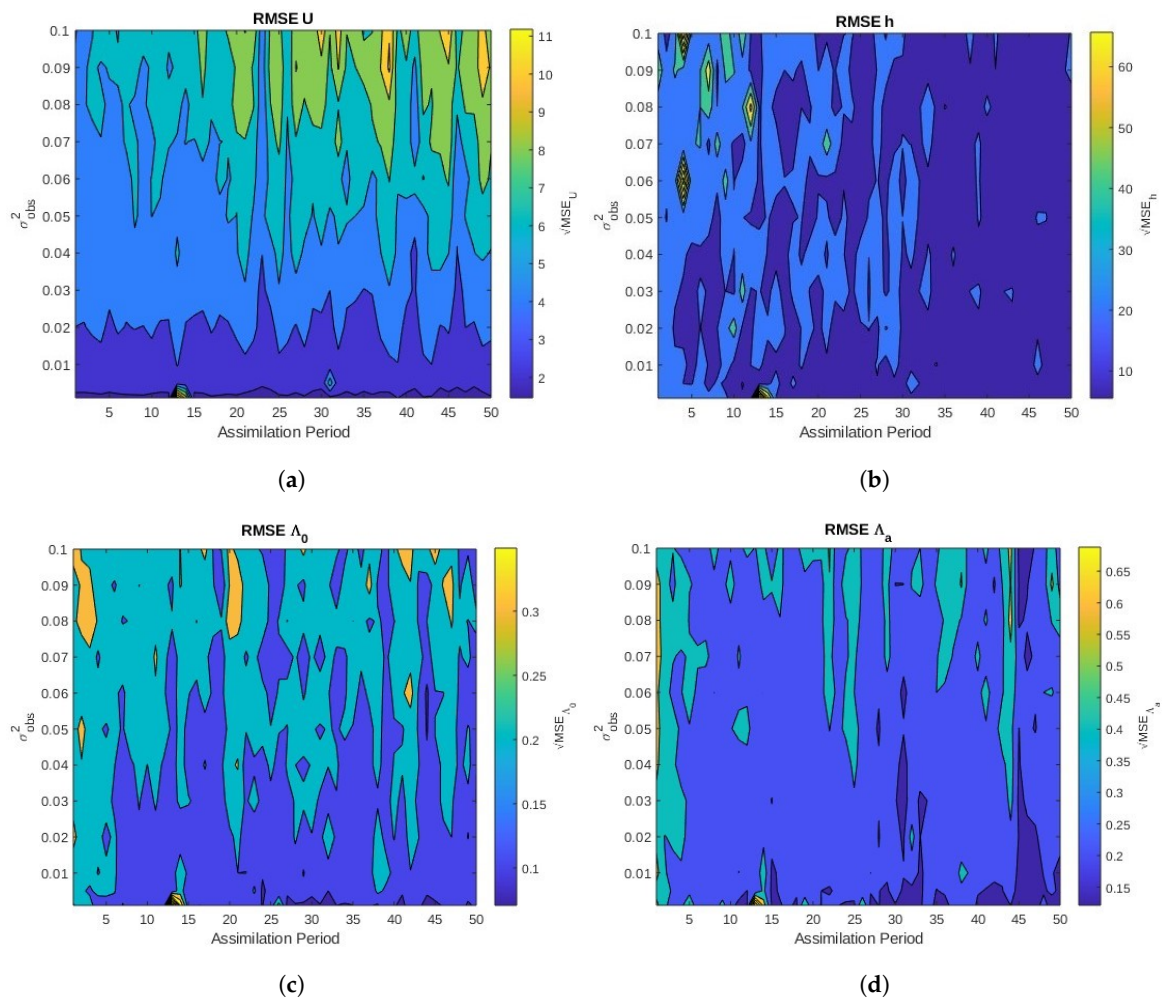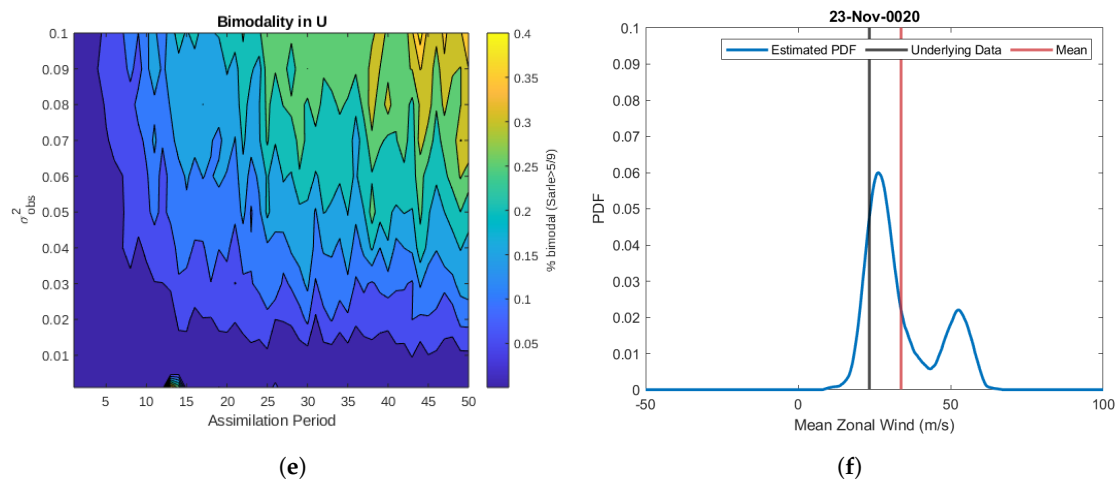

(a)

(b)

(c)

(d)

Figure 2. *Cont.*

(**e**)   (**f**)

Figure 2. (**a**–**d**) RMSEs for combinations of assimilation period and observation error when the state vector and control parameters h and Λ are estimated simultaneously using synthetic data from the Ruzmaikin model. (**e**) Bimodality as measured by the percentage of timepoints with sufficiently large Sarle statistic. (**f**) An example of a bimodal ensemble distribution with a Sarle statistic value of $BC = 0.728$, with $\sigma_{obs}^2 = 0.1$ and assimilation period of 3 weeks.

The relationship between RMSE and assimilation period, however, is a bit more nuanced, particularly for parameter estimation (for a fixed observation error, this corresponds to the horizontal slices in Figure 2). For state variable U, corresponding to zonal wind speed, it appears that the decreased number of observations yields to less accurate state estimations, particularly for large observation errors. However, this is not universally true, and even using just 2% of the available observations with an assimilation period of 50 days can still lead to nearly as good wind speed estimations when σ_{obs}^2 is small.

On the other hand, accuracy of parameter recovery appears to increase with increasing assimilation periods for h, Λ_0 and Λ_a. Indeed, Figure 2 shows that for a fixed observation error, RMSE of parameter estimates generally decreases with a longer time between observations/updates. This pattern is most prominent for estimation of h.

3.1.2. ECMWF Data Assimilation

It is now of interest to investigate the use of the particle filter to gain an understanding of stratospheric dynamics when "real-world" observations are used. To this end, fraternal twin experiments are conducted, where the "truth" is a smoothed version of the observed ECMWF mean zonal wind data described in Section 2.2. Gaussian white noise is added to be used as observations and the success of the particle filter at uncovering the smoothed data can be assessed. Thus, these experiments will investigate the ability of the model as well as the particle filter to produce an analysis similar to what is observed.

Results for varying assimilation periods and observation errors are shown in Figure 3. We not only show RMSE for state variable U (Figure 3a), but also estimates of parameters h, Λ_0, and Λ_a (Figure 3b–d). We note similarities in the RMSE profiles in these experiments with the identical twin experiments (Figure 2). However, the effects of increased assimilation periods on RMSE are no longer as apparent as in the twin model experiments. Now, to achieve the lowest RMSE for windspeeds, it is best to assimilate all the data, making daily updates. However, using our insights from the identical twin experiments, we expect that a reasonable value of h should be chosen from results with assimilation periods longer than one month (Figure 2b). Thus, Figure 3b may suggest an initial Rossby wave amplitude h between 60 and 120 m. These values lie within the region of bistability of the Ruzmaikin model (when $\Lambda = 1$ m/s/km is fixed). Similarly, by comparing Figure 2c,d with Figure 3c,d we estimate $\Lambda_0 \approx 0.1$ m/s/km and $\Lambda_a \approx 1.2$ m/s/km, which are significantly smaller than the values fixed in Ruzmaikin's model of 0.75 m/s/km and 2.25 m/s/km, respectively.
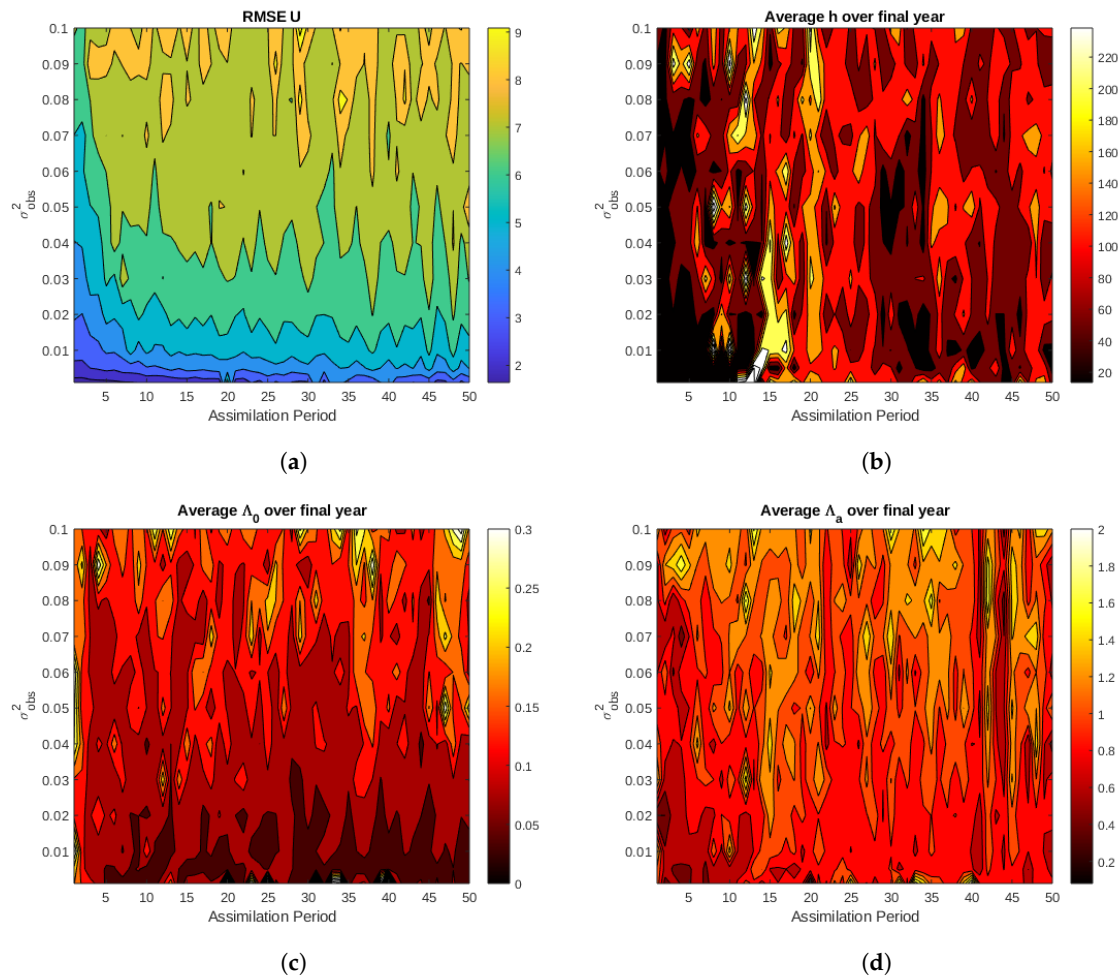
Figure 3. (**a**) RMSE for mean zonal wind using the particle filter with ECMWF reanalysis data. (**b**–**d**) Estimates for *h* and the coefficients of Λ obtained by time-averaging the ensemble mean over the last year of analysis.

3.1.3. Particle Filter Summary

An exploration of the particle filter was initially motivated by the expected bimodality of the zonal winds ensemble due to the bistability of the underlying model. We found that significant bimodality of the ensemble is achieved only for longer assimilation periods (Figure 2e), also corresponding to improved parameter estimates in identical twin experiments (Figure 2b). With short assimilation periods, frequent updates of the state variable *U* do not allow for the ensemble to spread out and sample both stable branches of the (h, U) bifurcation diagram. Further, it results in inferior parameter estimation, as the effects of the parameters are suppressed, with the analysis being driven by the observations and updates of *U*.

Applying these ideas to the ECMWF reanalysis data, we obtain estimates for *h* within the region of bistability when we utilize longer assimilation periods. For short assimilation periods, *h* is estimated as unrealistically small, again from the assimilation analysis being driven by the daily state updates, requiring tropospheric perturbations to play a less important role. However, even with updated parameter estimates, important phenomena including spikes in winter winds, are largely missed in our data assimilation. Thus, we find that a constant *h* is insufficient to capture the complex dynamics of the ECMWF reanalysis data, as its effects are being suppressed for short assimilation periods, and are unable to match the data for longer assimilation periods.

With this in mind, we turn to ESMDA, which avoids bias from updates to the state variables while also allowing for more flexibility in the parameter estimations, including

a time-dependent $h(t)$ and unparameterized $\Lambda(t)$. In this way, we allow for complexity to be added to the reduced order model such that it may better capture the higher-order dynamics represented in the ECMWF reanalysis data. Although it does not explicitly reveal which higher order terms or physical processes may be missing, their effects may be amalgamated into the existing parameters, thereby increasing the scope of processes described by h and Λ.

3.2. ESMDA Analysis

3.2.1. Free Parameters

Here we discuss the parameters we are able to estimate using the ESMDA scheme outlined in Section 2.3.2. We have several distinct scenarios to investigate with our parameter estimation. First, when $\Lambda(t)$ is parameterized as in Equation (5) with Λ_0, Λ_a, ϵ, and h constant and unknown. Second, when h is constant and unknown but $\Lambda(t)$, is replaced with an unparameterized vector, $\Lambda(t) \in \mathbb{R}^N$, where N is the number of days over which we have reanalysis data. Third, when $\Lambda(t)$ is as in the first case but h is replaced with a vector, $h(t) \in \mathbb{R}^N$, for a time dependent perturbation parameter and fourth, when both $\Lambda(t) \in \mathbb{R}^N$ and $h(t) \in \mathbb{R}^N$ so that they are both time dependent.

For each of the scenarios above we also estimate the initial conditions for X, Y, and U. In the cases where we allow for time-dependent Λ or h, we also have the choice of a decorrelation time τ_λ and τ_h. These parameters control how the vectors $\Lambda(t)$ and $h(t)$ are sampled. The initial sampling of these parameters is done by randomly sampling amplitudes and phases of sine and cosine terms penalizing shorter wavelengths according to a negative exponential and the decorrelation time described in Ref. [35,36]. The longer the decorrelation time, the more the shorter wavelengths are penalized in the sampling. As a result, the longer the decorrelation time, the smoother the time continuous priors for $\Lambda(t)$ and $h(t)$ will be. The decorrelation lengths are not estimated by the ESMDA analysis but are specified beforehand. In essence, when the decorrelation length is long, the randomly sampled 1-D prior curves—1000 of them in our case—for $\Lambda(t)$ and $h(t)$ vary slowly in time, which has the effect of an analysis curve that also varies slowly in time. In the case that the decorrelation length is small, the randomly sampled priors vary rapidly in time, allowing for an analysis curve that also does the same.

For the first case outlined above, we introduce an additional two shift parameters that will be estimated by the ESMDA analysis: c_{Λ_a} and c_ϵ. These parameters shift the sine functions in Equation (5) to align with the data. That is, $\Lambda(t)$ becomes,

$$\Lambda(t) = \Lambda_0 + \Lambda_a \sin\left(\frac{2\pi(t - c_{\Lambda_a})}{1 \text{ year}}\right) + \epsilon\Lambda_0 \sin^2\left(\frac{\pi(t - c_\epsilon)}{11 \text{ year}}\right). \tag{17}$$

We also have the freedom to assign observation errors to the reanalysis data. For the experiments reported on below, we set the standard deviation of the error in the winds as $\sigma_U = 10 \text{ m/s}$. We found in the identical twin model experiments, described below, that a larger observation error provided better estimates of $\Lambda(t)$ than with very low observation errors. A relatively large observation error also allows for parameter estimates to not be overly biased and to avoid spurious overfitting. We also found that RMSE ceases to improve for ensembles larger than about 1000 members, which is what we use for all ESMDA experiments in conjunction with 32 ESMDA steps.

3.2.2. Identical Twin Model Experiments

To evaluate the ESMDA scheme we first run a series of twin model experiments where our observational data is produced directly from our low order model. For this example we generate observational values of U using a fixed perturbation of $h = 68 \text{ m}$ and a $\Lambda(t)$ parameterized, as in Equation (5) with $\epsilon = 0.3$ and Λ_0, Λ_a, as prescribed in Ref. [17]. For these experiments we assume no prior structure on $\Lambda(t)$ or $h(t)$ and run ESMDA experiments across the chosen combinations of $\tau_\lambda = \{1.5, 1, 1/2, 1/4, 1/12, 1/24\}$ yr and $\tau_h = \{1.5, 1, 1/2, 1/4, 1/12, 1/24\}$ yr. We use these same values for each of the other

experiments when applicable. The values highlighted in this paper represent a subset of the values chosen for our experiments. We highlight values where changes in the analysis results are more apparent. We also avoid an extremely fine grained exploration of the decorellation length parameter space due to the computational cost. For simplicity, we denote these values in the manuscript with the closest integer number of days that they represent, specifically 547, 365, 182, 91, 30, and 15 days.

The results are summarized in Figure 4 where we show the root mean squared error (RMSE) for both $U(t)$ and $\Lambda(t)$ as well as the time-averaged value of $h(t)$, for which a good analysis should return a value close to $h = 68$ m. The summary results show that the best values for τ_λ are 547 and 365 days, while the results do not depend as much on τ_h, evidenced by the very similar values of RMSE for $U(t)$ and $\Lambda(t)$ for fixed values of τ_λ. It is also important to note that the lowest values of RMSE for $U(t)$ correspond to the lowest values of RMSE for $\Lambda(t)$ and the best average values of $h(t)$, despite only being conditioned on $U(t)$. This establishes, at least for these twin model experiments, some level of uniqueness in the analysis solution and a low risk of spurious parameter estimations that still produce good fits. For these experiments, we would expect that the longer decorrelation lengths for $\Lambda(t)$ would produce better results, considering that the period of $\Lambda(t)$ that produced the data is one year. As will be discussed later, this is not the case when assimilating the reanalysis data, which may suggest more variation in the real Earth system.
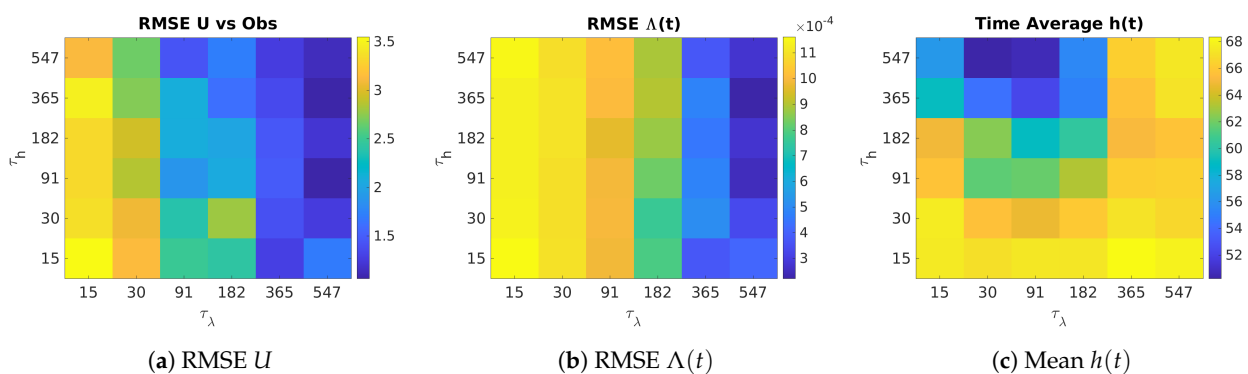

Figure 4. Summary statistics of ESMDA identical twin experiments for varying decorrelation lengths.

In Figure 5 we show three examples of the analyses we obtain for both $\Lambda(t)$ and $U(t)$ as well as the (Λ, U) phase space with the equilibrium solutions of the autonomous version of the system in Ref. [17]. The best fits for both $\Lambda(t)$ and $U(t)$ occur when $\tau_\lambda = 547$, which produces a phase space very similar to that in Ref. [17] for the same parameters used to generate the truth run. As τ_λ decreases, increased variation in $\Lambda(t)$ is observable, which translates into the phase space. The higher values of τ_λ also provide time-averaged values for $h(t)$ closest to the true value of $h = 68$ m.

While we only show the case where both $\Lambda(t)$ and $h(t)$ are free and time-dependent, other runs where h was kept constant but estimated with the ESMDA scheme show similar behavior typically obtaining analyses with $h \approx 68$ m for longer τ_λ. Truth run cases where h was set to 68 m and only $\Lambda(t)$ was estimated were also carried out. In this case, there was no significant improvement in the analyses when allowing both parameters to be free.

These twin model experiments establish three important points. First, the ESMDA scheme can successfully estimate parameters despite the high dimensionality resulting from time-dependent $\Lambda(t)$ and $h(t)$. Second, the best results as measured by the RMSE between analysis mean zonal wind and the true wind corresponds to the most accurate estimations of $\Lambda(t)$ and $h(t)$ rather than spurious parameter values that happen to produce good mean zonal wind analyses. Third, the decorrelation lengths have a strong effect on the quality of the analysis and must be considered. To that end, we range over the same values for the decorrelation lengths for all experiments using the ECMWF reanalysis data when a parameter is chosen to be time-dependent.
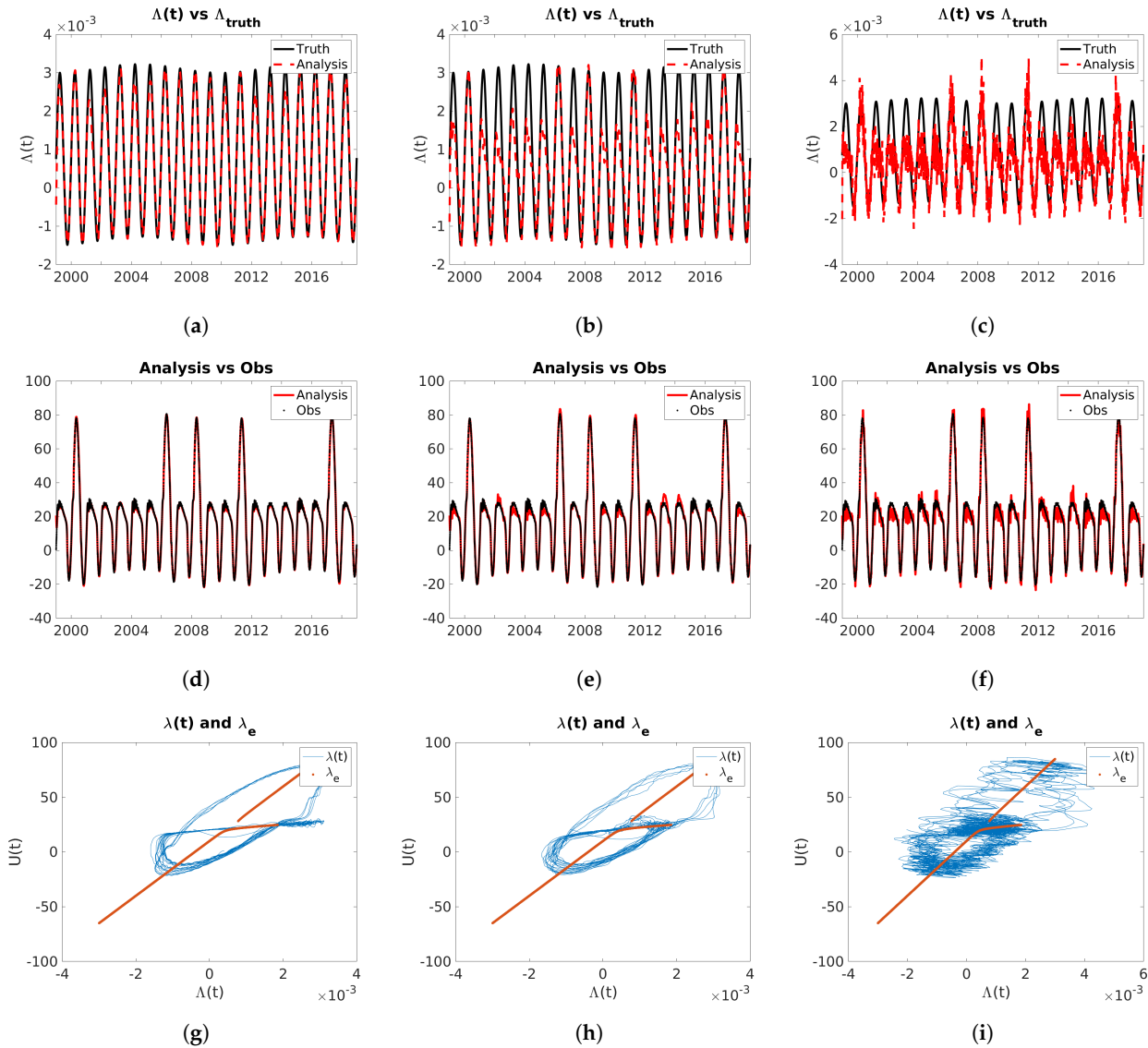
Figure 5. Example model outputs from the ESMDA identical twin experiments, each with $\tau_h = 91$. (**a**–**c**) show the model analysis $\Lambda(t)$ (red) versus the known, true $\Lambda(t)$ (black), while (**d**–**f**) show these curves for mean zonal wind speed $U(t)$. (**g**–**i**) Model output (blue) translated into $\Lambda - U$ phase space superimposed on the bifurcation diagram for Λ. Note that the bifurcation diagrams only showcases the stable equilibrium branches (orange), and this is repeated in subsequent figures. Decorrelation lengths for Λ are set at (**a**,**d**,**g**): $\tau_\lambda = 547$, (**b**,**e**,**h**): $\tau_\lambda = 182$, and (**c**,**f**,**i**): $\tau_\lambda = 15$.

3.2.3. Parameterized $\Lambda(t)$ and Free $h(t)$

In this section we explore whether or not only a time-dependent $h(t)$ can account for the variability observed in the ECMWF reanalysis data. In the reduced order models described in Refs. [17,21,37], recall that the perturbation parameter h is used to represent the effects of Rossby waves on the polar vortex. In these studies, a low value for h implies weaker Rossby waves and thus higher mean zonal winds while a large value of h gives rise to larger perturbations and lower mean zonal winds. In the autonomous version of the system in analyzed in Ref. [17], there is a region of bistability between values of $h \approx 25$ m and $h \approx 150$ m. We may expect to see (h, U) values close to the equilibrium branches shown in Ref. [17], Figure 3, in the phase space after assimilation of the ECMWF data. However, this is not what we typically see. The reason for this is that the mean zonal winds are typically much smaller in the data than those coming from the chosen parameters in the reduced order models.

Indeed, the bifurcation diagram for h in Ref. [17], Figure 3, results from fixing $\Lambda = 1$ m/s/km. However, as fixed Λ decreases, the region of bistability shrinks, until the stable branches converge to a single stable equilibrium around approximately $\Lambda \approx 0.5$ m/s/km, also reflected in Ref. [17], Figure 1. In our fit, Λ varies seasonally and is close to zero or negative during the summer.

Here, we take $\Lambda(t)$ as in Equation (17) but allow Λ_0, Λ_a, and ϵ to be free parameters estimated by ESMDA as well as the shift parameters, c_{Λ_a} and c_ϵ. Analysis results are shown in Figure 6. We find, as in the particle filter experiments, that the amplitude of $\Lambda(t)$ is much lower than the idealized cases explored in the various reduced order models. This can be observed in Figure 6e, where we see the phase space concentrated around $\Lambda = 0$. In all the assimilations for this case, recovery of the peaks in mean zonal wind was not achievable even when $h(t)$ had a very low decorrelation length to allow for more variability, which for this case corresponds to the lowest RMSE, shown in Figure 6a where we also note that the the variance of U decreases with the increasing τ_λ, as one might expect. In Figure 6b we see that the variance in $h(t)$ is correlated to the mean value with typically increasing variance as τ_h increases. In this case, when $h(t)$ is allowed to vary quickly in time, smaller changes are needed to cause variation in U while an $h(t)$ that cannot vary rapidly in time tends to need larger amplitude changes to affect U. The analysis curve can be compared to the observation in Figure 6d where we see good agreement in the troughs but a missing of the peaks. The resulting $\Lambda(t)$ from the fit parameters, estimated $h(t)$, and U are shown in Figure 6c. The example of assimilation results corresponds to $\tau_h = 15$, chosen because it provides the lowest RMSE value with mean zonal winds.
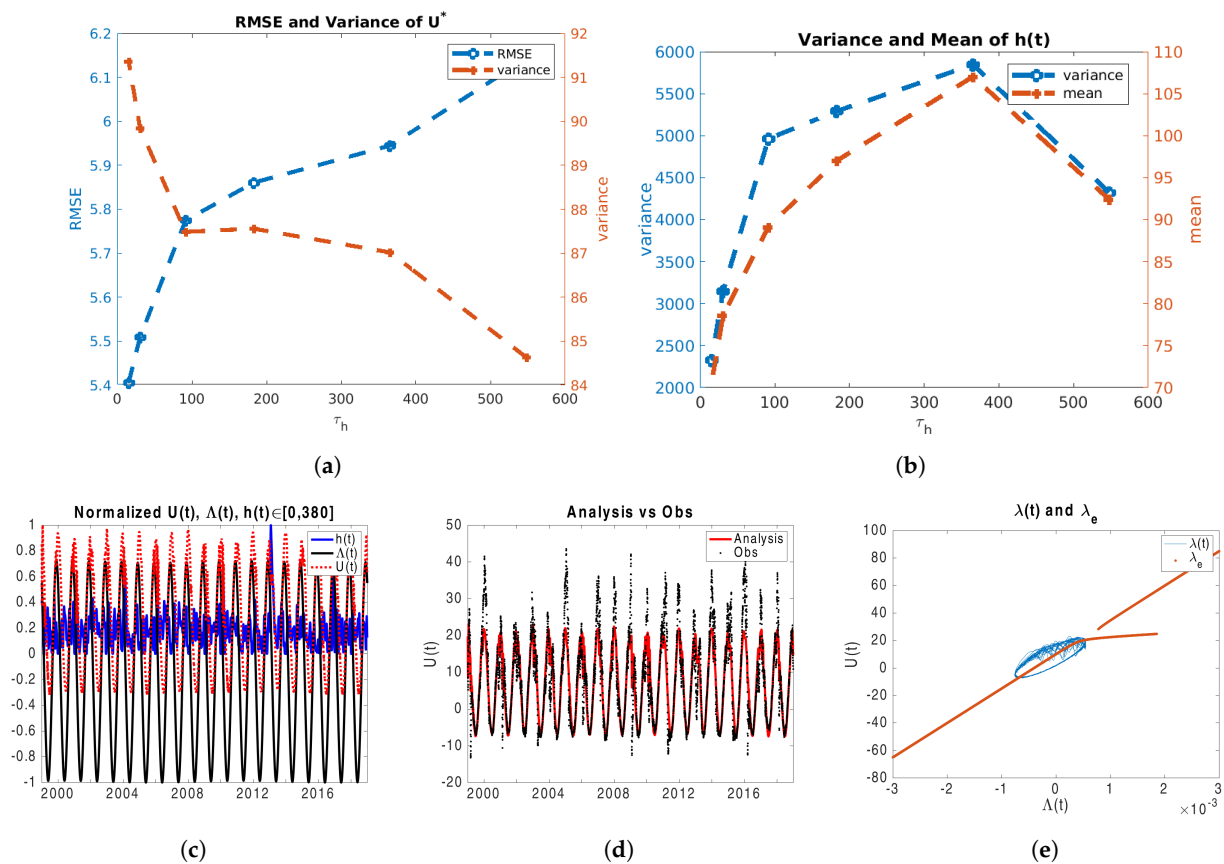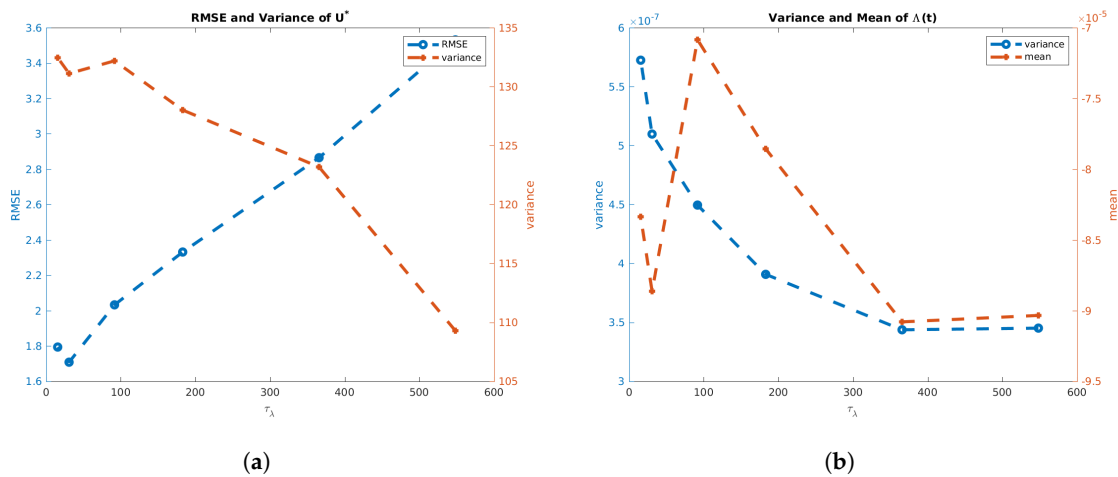

Figure 6. Results from ESMDA fraternal twin experiments for $\Lambda(t)$ parameterized by estimated Λ_0, Λ_a, and ϵ and $h(t)$ free. (**a**) RMSE (blue) and variance (orange) of model analysis $U(t)$, while (**b**) shows variance (blue) and mean (orange) of $h(t)$, each for varying values of τ_h. (**c**) Model output for normalized variables U, h, and Λ. (**d**) Comparison of estimated wind speeds (red) and observed wind speeds (black). (**e**) $\Lambda - U$ phase space of model output (blue) superimposed on the bifurcation diagram for Λ (orange). (**c–e**) Model output is from the lowest RMSE experiment ($\tau_h = 15$).

Due to the relatively small estimated amplitude of Λ and the inability to capture wintertime windspeeds, we also explored enforcing larger values for Λ_a. However, these assimilation experiments produced higher RMSE values by a factor of two, overshot the summertime troughs, and still failed to "jump" to the upper branch of the bifurcation diagram. The full results of this endeavor are presented in Appendix C.

3.2.4. Free $\Lambda(t)$ and Constant h

In the previous section, we observed that a time-dependent perturbation parameter $h(t)$ alone was insufficient to allow the Ruzmaikin model to accurately capture the ECMWF reanalysis data. In this section, we describe the results of our ESMDA experiments where we take h to be constant and estimate an unparameterized $\Lambda(t) \in \mathbb{R}^N$. We note that taking a constant h still allows for perturbations to the system and the estimation of a constant h is still informative in examining how well a reduced order model can represent realistic data. In general, we find that with only a time-dependent $\Lambda(t)$ estimated by the ESMDA scheme we achieve very good fits to the reanalysis data with the best fits occurring for lower values of τ_λ. This is in contrast to our truth runs where longer decorrelation lengths produced the best fits. However for those runs the prescribed $\Lambda(t)$ was slowly changing and correlated over long times, being represented by a sine wave with a period of 1 year. The fact that the lowest RMSE values occur for smaller τ_λ suggests that more variability in $\Lambda(t)$ is needed to account for some of the rapid changes in the reanalysis data. We show summary results for these experiments in Figure 7 where we see a general trend of increasing RMSE in $U(t)$ with decreasing variance in $\Lambda(t)$.

(**a**)   (**b**)

Figure 7. Results from ESMDA fraternal twin experiments for $\Lambda(t)$ free and $h(t)$ constant. (**a**) RMSE (blue) and variance (orange) of model analysis $U(t)$, while (**b**) shows the variance (blue) and mean (orange) of $\Lambda(t)$, each for varying values of τ_λ.

In Figure 8 we show the results of the ESMDA parameter estimation for $\tau_\lambda = [547, 182, 15]$ days. All show relatively good agreement with the reanalysis data with the smaller values of τ_λ providing the best fit to the extremes of mean zonal winds in the data Figure 8d–f. In Figure 8a–c corresponding to $\tau_\lambda = 30, 182$ and 547 respectively, we see a general trend of diminishing peaks and deeper troughs in $\Lambda(t)$ as τ_λ decreases. This trend also emerges in Figure 7b as the mean of $\Lambda(t)$ sharply decreases after $\tau_\lambda = 91$. Interestingly it is for these cases that the peaks of the mean zonal wind are best captured despite the generally lower values of $\Lambda(t)$. This may have to do with the ability of a more rapid and dynamic recovery in $\Lambda(t)$ after a large dip permitted when τ_λ is small. We also find that relatively low values of h are estimated with $h \approx 35$ m in these cases. This is likely due to the generally lower mean zonal winds represented in the data as opposed to the idealized cases examined in Ref. [17].
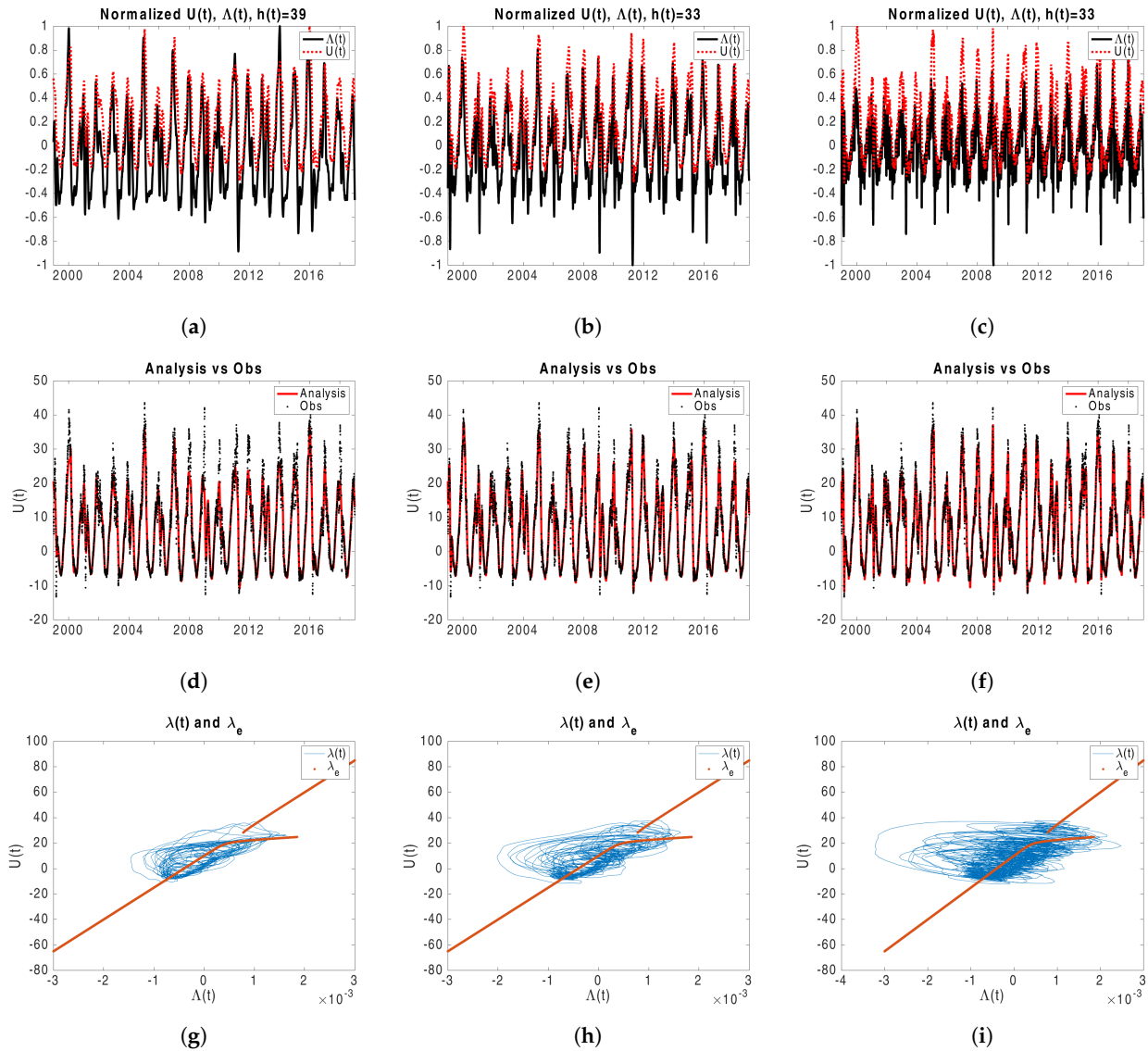
Figure 8. Example model results for $\Lambda(t)$ free and h constant. (**a–c**) Model output for normalized variables U (red) and Λ (black). (**d–f**) Comparison of model estimated wind speeds (red) with the observed wind speeds (black). (**g–i**) $\Lambda - U$ phase space of model output (blue) superimposed on the bifurcation diagram for Λ (orange). Decorrelation lengths for Λ are set at (**a,d,g**): $\tau_\lambda = 547$, (**b,e,h**): $\tau_\lambda = 182$, and (**c,f,i**): $\tau_\lambda = 30$.

In Figure 8g–i, we show the $(\Lambda(t), U(t))$ phase space with the equilibrium solutions of the autonomous system in Ref. [17]. The phase space orbits the equilibrium solutions with the most time spent on the lower branch and some jumps to the upper stable branch. The fact that the phase space is so similar to the idealized time-dependent case in Ref. [17] and Figure 5g–i demonstrates that the parameters required to accurately match the reanalysis data are not overly dynamically different from the idealized case. This also suggests that the reduced order model captures the most important physics of the real system.

3.2.5. Free $\Lambda(t)$ and $h(t)$

Here, we allow both parameters to be free, as in the identical twin model experiments. As in the twin model case, we typically find that RMSE for the mean zonal wind is not very dependent on τ_h but strongly dependent on τ_λ as can be seen in Figure 9a. Unlike the identical twin model case, the lowest values for mean zonal RMSE occur for lower values of τ_λ, and this suggests that more variability in $\Lambda(t)$ is required to match the ECMWF reanalysis data. As might be expected as τ_λ decreases the variance in both $\Lambda(t)$ and $U(t)$

increase, shown in Figure 9b,c. In Figure 9d we see the that variance in $h(t)$ decreases as τ_λ decreases, suggesting that the model is most sensitive to $\Lambda(t)$. It is for the cases that $h(t)$ varies less and $\Lambda(t)$ varies more we achieve the lowest values in RMSE for the mean zonal wind. In all cases we are able to capture the peaks fairly well and extremely well for small τ_λ.

(**a**) RMSE U

(**b**) U Variance

(**c**) $\Lambda(t)$ Variance

(**d**) $h(t)$ Variance
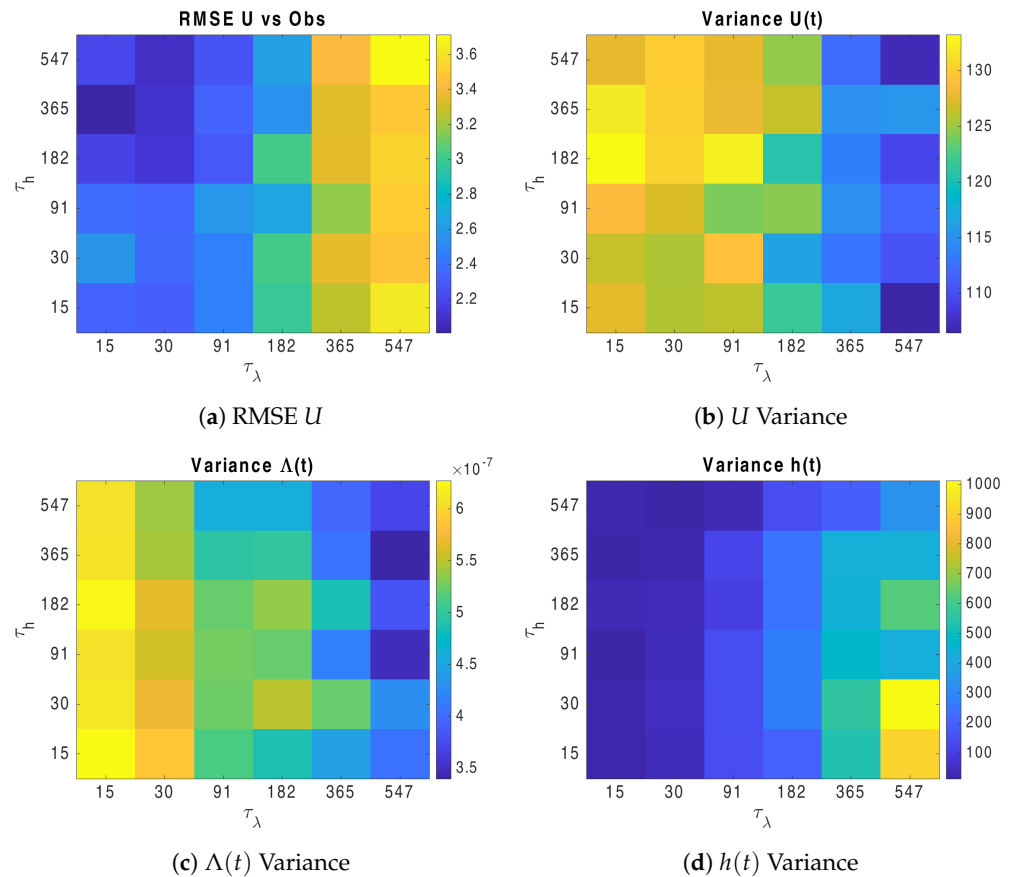
Figure 9. Summary statistics for ESMDA fraternal twin experiments with free $\Lambda(t)$ and $h(t)$ and varying decorrelation lengths.

In Figure 10 we show three examples from these experiments for a fixed τ_h as the results were not sensitive to that parameter. It is is also notable how similar these results are to those in the previous section where h was fixed. A visual inspection between Figures 8 and 10 shows this with nearly identical results and extremely similar phase spaces.

In Figure 10a–c we see that the estimated $h(t)$ takes on a wider range of values when τ_λ is large than when τ_λ is small. Allowing h to be time-dependent does provide slightly smaller RMSE values—but not by much. As $\Lambda(t)$ is allowed to be more dynamic it appears that $h(t)$ needs to do "less work" for a good data match.

3.3. Analysis Around SSW Events

As part of our analysis on how representative reduced order models of the polar vortex can be, we compare our analysis curves to a list of known sudden stratospheric warming (SSW) events taken from Ref. [38]. To do this, we take snapshots of the analysis curves 28 days before and after the specified SSW event looking at $\Lambda(t)$, $h(t)$, and $U(t)$. We show snapshots of $\Lambda(t)$ and $h(t)$ for six cases, specifically with $\tau_h = 365$ and $\tau_\lambda = 547, 182$, and 15 as well as with $\tau_h = 15$ and the same list of τ_λ above for three different SSW events and with more dates shown in Appendix D. We would expect to see a sudden drop in $\Lambda(t)$ either from normal waves from below propagating up into the upper layers, causing winds to slow and stratospheric temperatures to increase, or a rapid reduction in the thermal gradient between the lower and upper latitudes in the stratosphere (Equation (4))—or perhaps a combination of

both. We might also expect to see a rapid increase in $h(t)$, which would correspond to more normal waves propagating up into the upper layers. In all of these cases, we would expect the event to be followed by a drop in mean zonal winds with a slow or very little recovery in the 28 days after the event. In general, this behavior is in line with timelines for and definitions of various events dubbed SSW events [39].
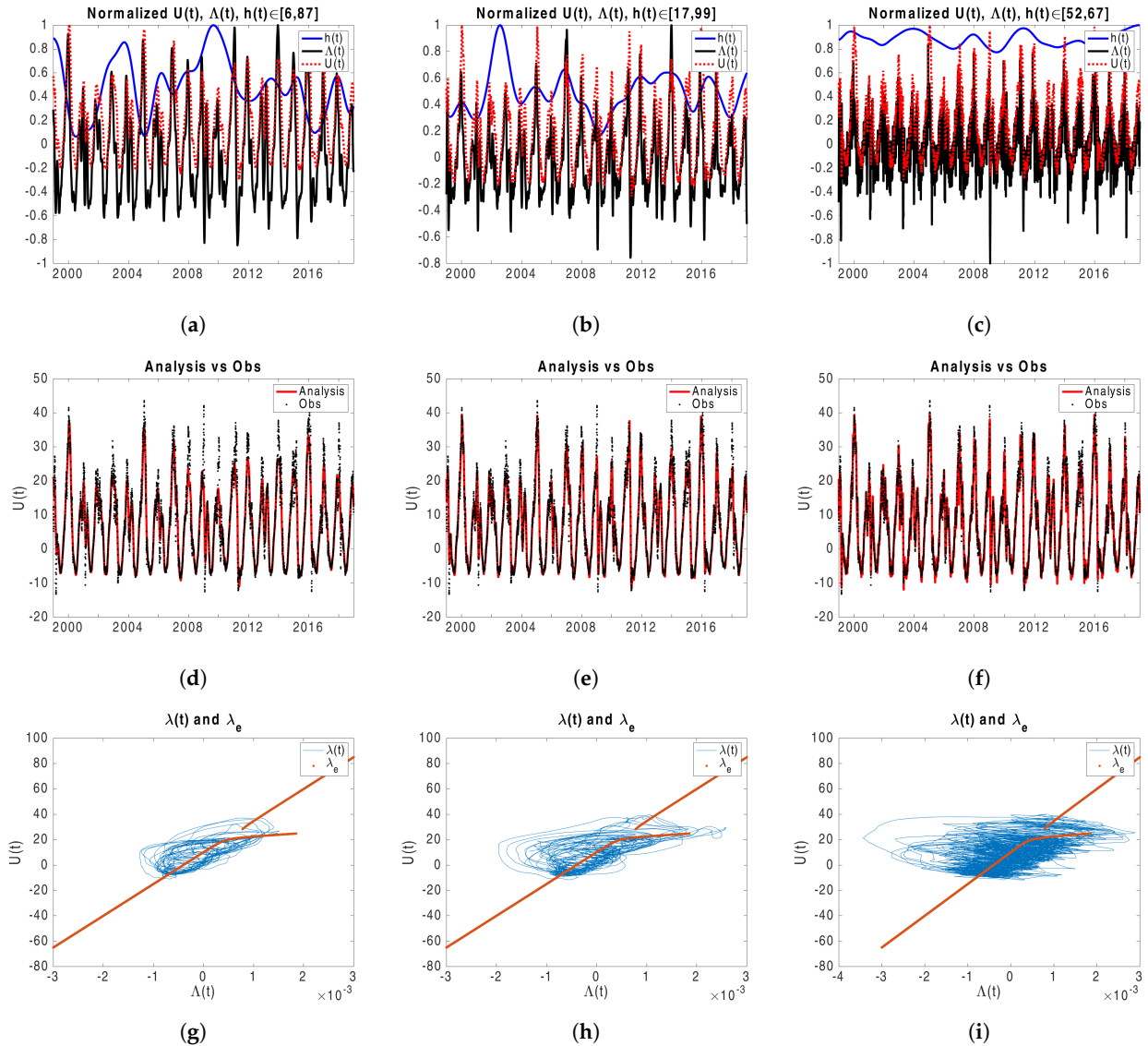

Figure 10. Example model results with both $\Lambda(t)$ and $h(t)$ free and $\tau_h = 365$. (**a**–**c**) Model output for normalized variables U (red), h (blue), and Λ (black). (**d**–**f**) Comparison of model estimated wind speeds (red) with the observed wind speeds (black). (**g**–**i**) $\Lambda - U$ phase space of model output superimposed on the bifurcation diagram for Λ. Decorrelation lengths for Λ are set at (**a**,**d**,**g**): $\tau_\lambda = 547$, (**b**,**e**,**h**): $\tau_\lambda = 182$, and (**c**,**f**,**i**): $\tau_\lambda = 15$.

In general, a rapid decrease in $\Lambda(t)$ is what we observe throughout all of our experiments where it is estimated completely by the ESMDA scheme. The described pattern is most noticeable for shorter τ_λ but does persist for longer decorrelation lengths while not being sensitive to τ_h. However, the expected rapid increase in $h(t)$ is only a persistent phenomena when $\tau_h = 15$ days and is almost nonexistent for the longer decorrelation lengths. Nevertheless, we note that as long as $h(t)$ is not zero, normal wave perturbations are considered to be occurring.

In Figure 11, we show examples of these snapshots for three selected dates with $\tau_\lambda = 547, 182,$ and 15 and $\tau_h = 365$. For the majority of the SSW events examined, $\Lambda(t)$

exhibits a convex shape with a minimum near the listed date of the SSW and a recovery thereafter. With $\tau_h = 365$ in this case we see very little change in $h(t)$ due to the long decorellation length constraining the variability of the $h(t)$ prior samples. In this case $\Lambda(t)$ is doing most of the forcing in the model. The mean zonal wind exhibits a delayed decrease with no significant recovery in the 28-day period following the listed SSW date. When τ_λ is small enough the $\Lambda(t)$ becomes less smooth and more dynamic but still exhibits the same general pattern. We also see that for smaller τ_λ the minimum value of $\Lambda(t)$ becomes more extreme for the majority of cases. This is because for small decorrelation lengths the priors for $\Lambda(t)$ are not tied to values far in the past or future and can respond quickly to rapid changes in the data.
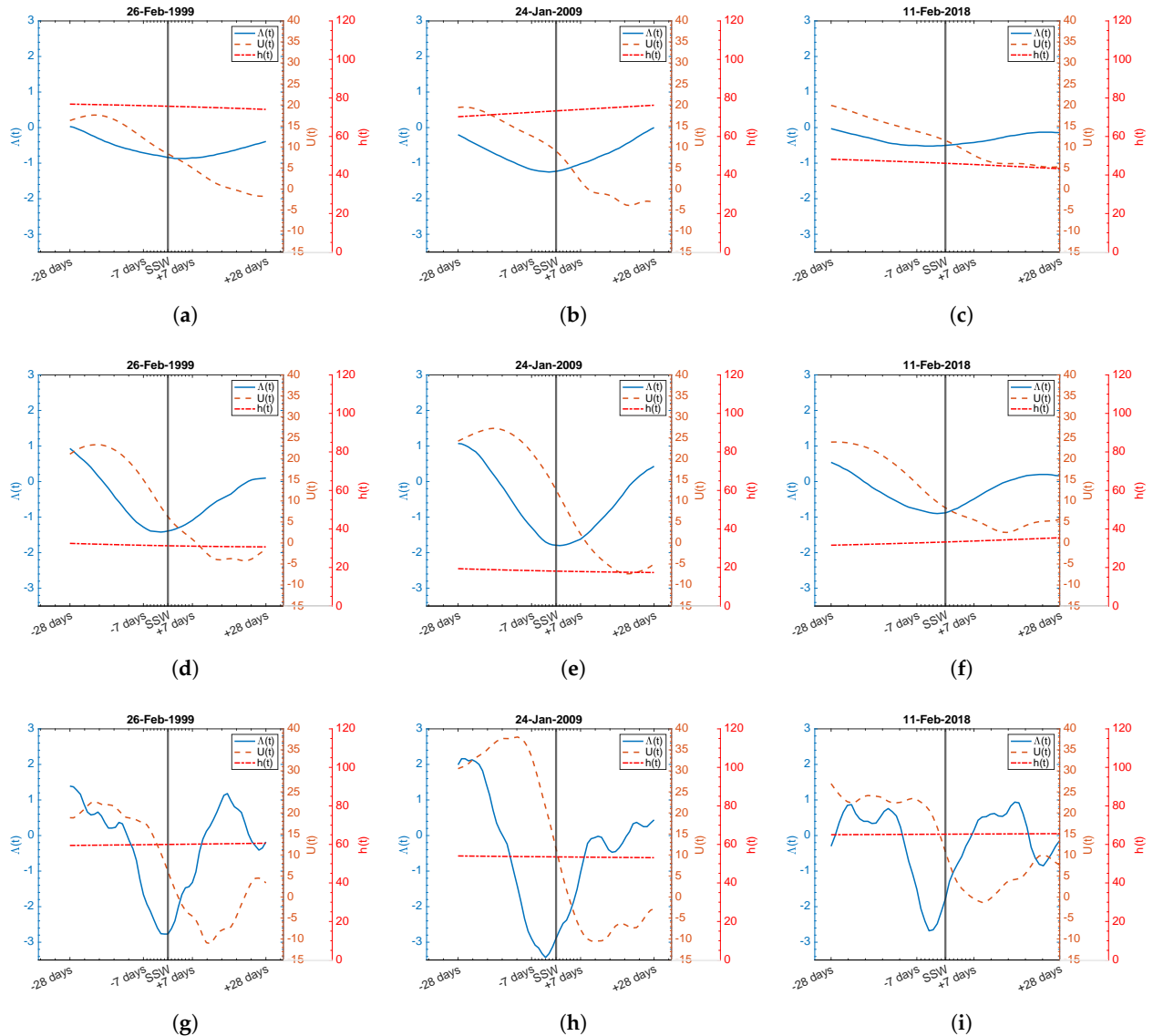
Figure 11. Examples of model output around known SSW events for U (orange), Λ (blue), and h (red), each with $\tau_h = 365$. Decorrelation lengths for Λ are set at (**a–c**): $\tau_\lambda = 547$, (**d–f**): $\tau_\lambda = 182$, and (**g–i**): $\tau_\lambda = 15$.

In Figure 12 we show snapshots for the same dates and values of τ_λ but with $\tau_h = 15$. With $\tau_h = 15$ the ensemble of priors used in the ESMDA scheme all have more variability allowing for a more variable analysis curve. In this case we see a very similar pattern as previously for $\Lambda(t)$ but a much more variable response for $h(t)$. We see a typical pattern of at least a rapid increase in $h(t)$ right before the SSW event, perhaps most strikingly with the Feburary 2018 SSW. We show the snapshots for all dates listed in Ref. [38] with $\tau_h = 15$
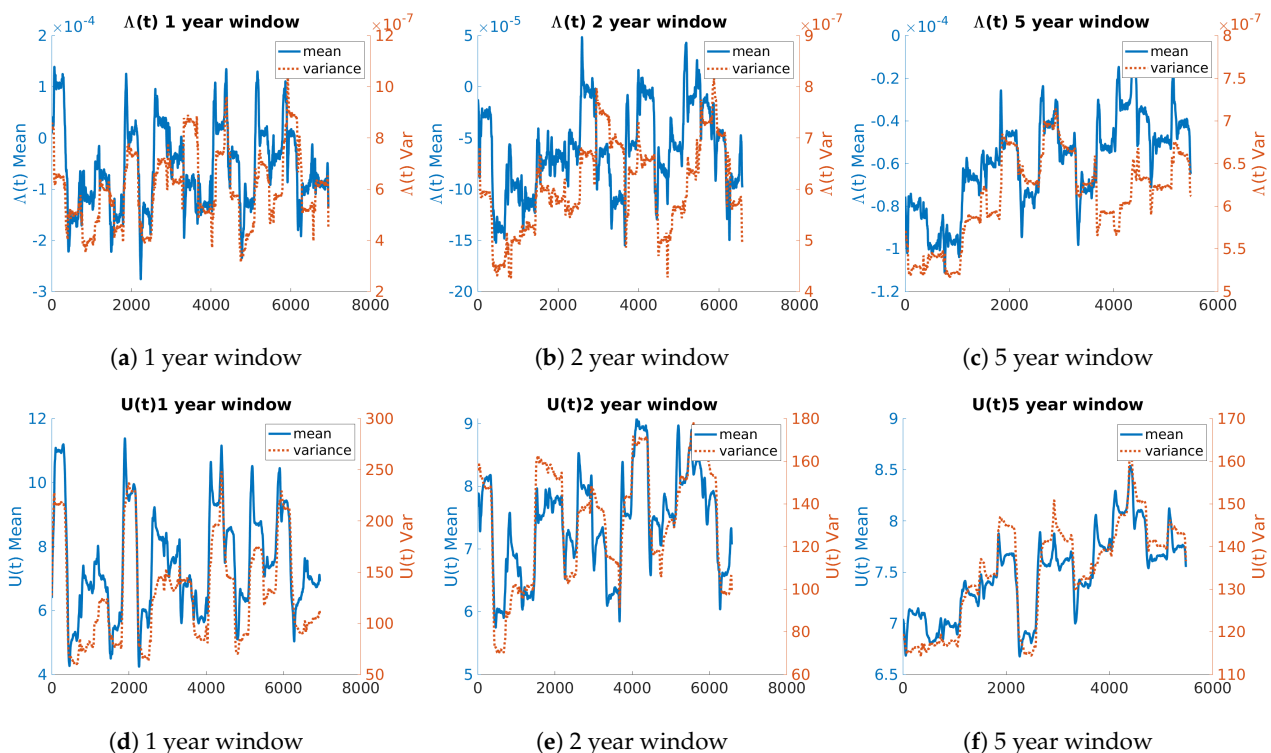
in Figure A3 (for $\tau_\lambda = 547$), Figure A4 (for $\tau_\lambda = 182$), and Figure A5 (for $\tau_\lambda = 15$). It is noteworthy that the general pattern observed in these snapshots only emerges for shorter τ_λ on the 24 March 2010, SSW event. This may be related to the proximity of the previous SSW event on 9 February 2010 just 43 days before and its proximity to the end of winter. As in Ref. [40], no day within 20 days of a previous SSW should be considered a separate event and the final warming must also take place before 30 April. The February 2007 event is also unusual in that the general pattern emerges only for shorter τ_λ and exhibits a somewhat rapid recovery in the mean zonal wind. This may be attributable to a noticeably higher average mean zonal wind that year around the event [41]. A strong latitudinal thermal gradient, associated with a strong vortex, may allow for a faster recovery of the wind speed. We would also like to highlight that the magnitude in the change of $h(t)$ around these events is larger when τ_λ is longer. This again is because when the decorrelation length for $\Lambda(t)$ is long the priors sampled for the ESMDA scheme will have less variability and can therefore do "less work" in forcing the system, while if the decorrelation length is small for $h(t)$ its priors will be more variable and can do "more work" when forcing the system.
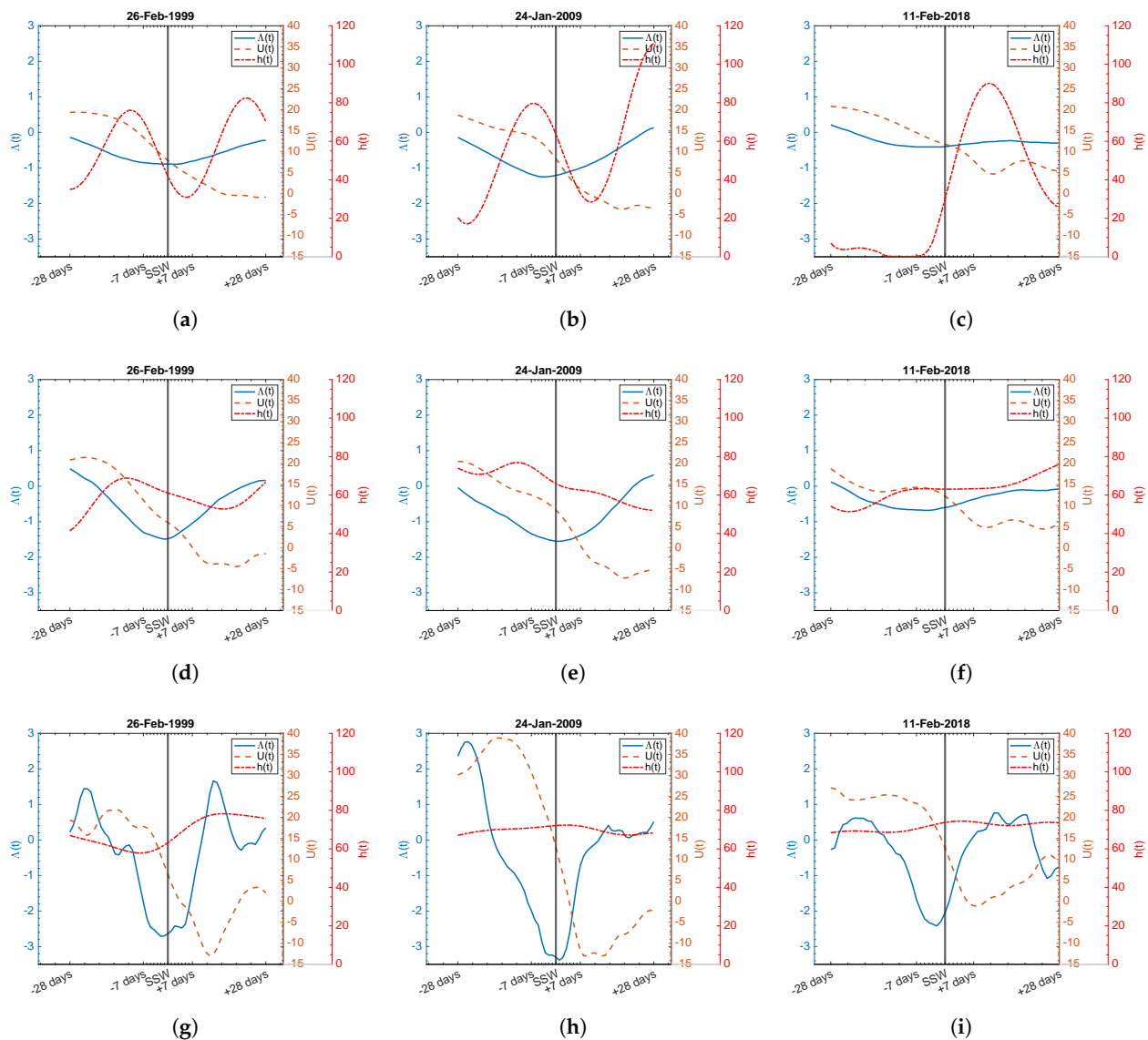
Figure 12. Examples of model output around known SSW events for U (orange), Λ (blue), and h (red), each with $\tau_h = 15$. Decorrelation lengths for Λ are set at (**a–c**): $\tau_\lambda = 547$, (**d–f**): $\tau_\lambda = 182$, and (**g–i**): $\tau_\lambda = 15$.

The generally accepted cause of an SSW event is due to atmospheric waves that originate in the troposphere, which propagate upward, weakening the stratospheric jet. In this analysis, when τ_h is small enough we do see rapid increases in $h(t)$, which would correspond to increased perturbation due to waves. However, we are still able to capture the decrease in winds and match the data well when τ_h is longer and this behavior is not present, although because $h \neq 0$, perturbation is still present. As mentioned in earlier sections, we were only able to match the reanalysis data well when $\Lambda(t)$ is estimated by the ESMDA scheme, and this holds true for the SSW events. This perhaps suggests that more complexity is needed in this model to be able to produce the kinds of variability we see in the reanalysis data. While the scope of this paper is simply to evaluate if this reduced order model can produce observed variability and what it takes to do so, it would be interesting to explore modified versions of the model. In particular, taking the vertical wind shear to be a function of both time and h, as $\Lambda(t, h)$ could be the aim of future work. Nonetheless, these results are interesting as they show that the ESMDA estimated reduced order model parameters respond appropriately to real physical events. That is, despite the generality added by free and unparameterized $\Lambda(t)$ and $h(t)$, the recovered parameters are in line with what may be expected to emerge during an SSW event.

Finally, we comment on some trends observed in the analysis data. We computed 1 year, 2 year, and 5 year moving averages and variances for the analysis $\Lambda(t)$ and $U(t)$. In general, there was a noticeable upward trend for both, which becomes more pronounced for the longer windows. While these trends are not definitive, they may suggest shifts in the behavior of the polar vortex over the 20-year dataset considered. We show an example of these trends in Figure 13.

(**a**) 1 year window   (**b**) 2 year window   (**c**) 5 year window

(**d**) 1 year window   (**e**) 2 year window   (**f**) 5 year window

Figure 13. Mean (blue) and variance (orange) of (**a**–**c**): $\Lambda(t)$ and (**d**–**f**): $U(t)$ over several different moving windows, 1 year, 2 years, and 5 years.

4. Conclusions and Discussion

In this manuscript, we demonstrated that reduced order models of stratospheric wave–zonal interactions, in particular the Ruzmaikin model (2003) in conjunction with data assimilation schemes, can be used to produce model output closely matches with averaged ERA-Interim reanalysis data. We employed a 20-year dataset of atmospheric reanalysis data sourced from the ECMWF for the purpose of understanding the behavior and influence of

physically-based control parameters of the low order model in the context of real-world phenomena. Initially, we applied a particle filter due to the assumed bimodality of the ensemble associated with bistability of the model and of the winter polar vortex. Yet, this method ultimately failed to capture several relevant features of the data, and subsequently, we utilized ESMDA techniques to allow for added complexity of parameters.

When using the particle filter, we determined the influence of hyperparameters through identical twin model experiments. We confirmed that lower observation error results in better estimation of state variables and parameters. However, the effects of longer assimilation periods was initially surprising, as we found that assimilating less data can actually improve parameter estimation. One reason this may be the case is that the ODE model is given more time to "feel" the influence of the parameter updates. With short assimilation periods, the parameters show much larger variances, which may come from over-fitting the data.

We used fraternal twin experiments to determine how well the reduced order model could recover ECMWF reanalysis data using the particle filter algorithm. We noted similarities in the RMSE profiles with the identical twin experiments. However, even with the updated parameter estimates, important phenomena related to the winter polar vortex are largely missed in our data assimilation. Thus, ESMDA was employed to explore the applicability of the Ruzmaikin model when h and Λ are allowed to be fully free to vary with respect to time, rather than being prescribed in a fixed form.

We had several distinct scenarios to investigate using ESMDA. First, when $\Lambda(t)$ is parameterized as in Equation (5) with Λ_0, Λ_a, ϵ, and h constant and unknown. Second, when h is constant and unknown but $\Lambda(t)$ is unparameterized and free. Third, when $\Lambda(t)$ is as in the first case but h is replaced with an unparameterized, free vector, $h(t)$ for a time-dependent perturbation parameter and fourth, when both $\Lambda(t)$ and $h(t)$ are both time-dependent and unparameterized. In the cases where we allowed for time-dependent Λ or h, we also had the choice of a decorrelation time τ_λ and τ_h.

To evaluate the ESMDA scheme, we conducted a series of identical twin model experiments, as in the case of the particle filter, where observational data was produced directly from the low order model. Overall, using ESMDA, we concluded that a free $\Lambda(t)$ and $h(t)$ and sampling the space of reasonable decorrelation lengths provided an improvement in data fitting, with the best results coming from relatively long decorrelation lengths for h. Furthermore, the recovered parameters that closely matched the reanalysis data was in line with the idealized situations considered in Ref. [17] with the time-dependent $(\Lambda(t), U(t))$ phase space orbiting the stable equilbrium branches of an even further simplified autonomous version of the reduced order model.

We also examined our analysis curves around some known SSW events, finding a general pattern in $\Lambda(t)$, $h(t)$, and $U(t)$ consistent with expectations for such an event. However, we note that a rapid increase in $h(t)$, corresponding to abnormal normal wave propagation, was not absolutely necessary to capture the SSW in terms of a drop in $\Lambda(t)$ and $U(t)$. This could mean that there is room for added complexity in the model, perhaps adding a dependence on h to Λ. Data-driven methods could be used to investigate this and may be the aim of future work. We also noticed a general increasing trend in the moving averages and variances of $\Lambda(t)$ and $U(t)$, which may be a result of increasing tropospheric and decreasing stratospheric temperatures resulting from increased CO_2 levels in the atmosphere. It has been understood that increases in global CO_2 lead to increases in tropospheric temperatures and decreases in stratospheric temperatures as a warmer surface pushes the edge of the stratosphere higher [42]. Evidence of such a signature of increasing CO_2 levels has been observed in data [43]. A cooler stratosphere may cause stronger temperature gradients, leading to generally higher mean zonal winds and more variability.

Author Contributions: Project conceptualization and supervision by C.K.R.T.J., ECMWF data processing and Figure 1 by Z.W. Particle filter analysis and visualizations by J.S. ESMDA core algorithm coded by Z.W., with edits and analysis by C.S. and E.F., and visualizations by C.S. Main manuscript

Appendix A

In this section, we go through the derivation of the reduced order model by Ruzmaikin et al. [17] from the original Holton and Mass model [6].

The HM76 model is a quasi-geostrophic β-plane channel model, which is similar to the one used by Geisler (1974) to study the essential dynamics of sudden stratospheric warming. Holton and Mass modified Geisler's model by adding a sine jet meridional variation to reflect the mean zonal flow's dependence on latitude, while Geisler assumed a zonal flow that is independent of latitude. This sine jet profile roughly models the observed polar night jet in the Northern Hemisphere and is associated with vertical forcing from planetary waves. HM76 assumes that the main driving forces of mean zonal circulation are differential radiative heating and horizontal eddy heat fluxes caused by vertically propagating planetary waves. The mean zonal wind $\bar{u}$ and the geostrophic streamfunction of a wave ψ' are assumed to take the following forms by Holton and Mass (1976):

$$\bar{u}(y,z,t) = U(z,t)\sin\ell y,$$
$$\psi'(x,y,z,t) = \mathrm{Re}\left[\Psi(z,t)e^{ikx}\right]e^{z/2H}\sin\ell y, \tag{A1}$$

where k, ℓ are wavenumbers for x, y the standard azimuthal and latitudinal coordinates. Here f_0 is the Coriolis parameter at $60°$ N ($f_0 = 1.26 \times 10^{-4}\mathrm{s}^{-2}$) and H is a mean scale height ($H = 7$ km). Notice that the variable Ψ is complex valued. Holton and Mass also further assumed that the wave fields are governed by the linearized quasi-geostrophic potential vorticity equation in log pressure coordinates:

$$\left(\frac{\partial}{\partial t} + \bar{u}\frac{\partial}{\partial x}\right)q' + \beta'\frac{\partial\psi'}{\partial x} + \frac{f_0^2}{\rho}\frac{\partial}{\partial z}\left(\frac{\alpha\rho}{N^2}\frac{\partial\psi'}{\partial z}\right) = 0, \tag{A2}$$

where

$$q' = \nabla^2\psi' + \frac{f_0^2}{\rho}\frac{\partial}{\partial z}\left(\frac{\rho}{N^2}\frac{\partial\psi'}{\partial z}\right) \tag{A3}$$

represents the perturbation potential vorticity and

$$\beta' = \beta - \frac{\partial^2\bar{u}}{\partial y^2} - \frac{f_0^2}{\rho}\frac{\partial}{\partial z}\left(\frac{\rho}{N^2}\frac{\partial\bar{u}}{\partial z}\right) \tag{A4}$$

represents the gradient of the basic state potential vorticity. Here, β is the meridional derivative of the Coriolis parameter at $60°$ N, which is 1.14×10^{-11} s^{-1}m^{-1}, N^2 is the buoyancy parameter fixed at $N^2 = 4 \times 10^{-4}$ s^{-2}, $\rho = \rho_0 \times \exp(-z/H)$ is a standard density, and $\alpha = \alpha(z)$ is a Newtonian cooling rate coefficient.

The prognostic equation of the mean zonal flow is given by Ref. [6]:

$$\frac{\partial}{\partial t}\left[\frac{\partial^2 \bar{u}}{\partial y^2} + \frac{f_0^2}{N^2}\frac{1}{\rho}\frac{\partial}{\partial z}\left(\rho\frac{\partial \bar{u}}{\partial z}\right)\right] = -\frac{f_0^2}{N^2}\frac{1}{\rho}\frac{\partial}{\partial z}\left[\alpha\rho\frac{\partial(\bar{u} - u_R)}{\partial z}\right] + \frac{f_0^2}{N^2}\frac{\partial^2}{\partial y^2}\left[\frac{1}{\rho}\frac{\partial}{\partial z}\left(\rho v'\frac{\partial \psi'}{\partial z}\right)\right], \tag{A5}$$

where $v' = \partial\psi'/\partial x$ and $\bar{u}$ is the mean zonal flow obtained by averaging over x. The flow is assumed to be confined to a β-channel centered at $60°$N with meridional extent L of $60°$ latitude. We substitute the assumed form of solutions (Equation A1) into Equations (A2) and (A5). Then, the linearized quasi-geostrophic potential vorticity equation and mean-flow equation become, respectively

$$\left(\frac{\partial}{\partial t} + ik\epsilon U\right)\left[-(k^2 + \ell^2) + \frac{f_0^2}{N^2}\left(\frac{\partial^2}{\partial z^2} - \frac{1}{4H^2}\right)\right]\Psi + \beta_e' ik\Psi$$
$$+ \frac{f_0^2}{N^2}\left(\frac{\partial}{\partial z} - \frac{1}{2H}\right)\left[\alpha\left(\frac{\partial}{\partial z} + \frac{1}{2H}\right)\right] = 0, \tag{A6}$$

$$\frac{1}{\epsilon}\frac{\partial\beta_e'}{\partial t} = \frac{f_0^2}{N^2}\left(\frac{\partial}{\partial z} - \frac{1}{H}\right)\left[\alpha\left(\frac{\partial U}{\partial z} - \frac{dU_R}{dz}\right)\right] + \frac{1}{2}k\ell^2\epsilon\frac{f_0^2}{N^2}e^{z/H}\text{Im}\left[\Psi^*\frac{\partial^2\Psi}{\partial z^2}\right], \tag{A7}$$

where

$$\beta_e' = \beta + \ell^2\epsilon U - \epsilon\frac{f_0^2}{N^2}\left(\frac{\partial^2 U}{\partial z^2} - \frac{1}{H}\frac{\partial U}{\partial z}\right). \tag{A8}$$

A constant $\epsilon = 8/(3\pi)$ is derived from the truncation of nonlinear term $\sin^2 \ell y$ using Fourier time series. With the specific localization of the β-channel, $\ell = 3/a = 4.71 \times 10^{-7}$ m^{-1} and $k = 2/(a\cos\pi/3) = 6.28 \times 10^{-7}$ m^{-1} where a is the radius of the earth. For the boundary conditions, [6] assumes zero normal flow across the lateral boundaries, which requires that ψ' and v' vanish at the side boundary $y = 0, L$. The upper and bottom boundaries are chosen at $z_B = 10$ km (tropopause) and $z_T = 80$ km (mesopause), respectively. Further, Ref. [6] assumes that pertubation and zonal mean flow vanish at the upper boundary and specifies the lower boundary conditions by setting $\bar{u} = \bar{u}_B(y)$ and $\psi' = \psi_B(y, t)$.

Yoden then developed a simplified version of Ref. [6] in 1987 and 1990. Ref. [37] simplified Ref. [6] by using central finite differencing for Ψ and U, thus reducing (A6) and (A7) to 81 nonlinear ordinary differential equations. Ref. [37] changes the bottom boundary to 0 km instead of the tropopause and specifies the bottom and top boundary conditions as

$$\Psi(z_T, t) = 0$$
$$\frac{\partial U}{\partial z}\Big|_{z=z_T} = \frac{dU_R}{dz}\Big|_{z=z_T}$$
$$\Psi(0, t) = gh_B(t)/f_0 \tag{A9}$$
$$U(0, t) = U_R(0),$$

where h_B plays the same role as $h(t)$ in Ref. [6] but is assumed to be constant in Yoden's studies. For the radiative equilibrium U_R, Ref. [37] uses the same simple linear model suggested by Ref. [44]:

$$U_R(z, t) = U_{RB} + \Lambda(t)z \tag{A10}$$

where Yoden fixed U_{RB} to 10 m s^{-1} and Λ at 2 m s^{-1}/km. Hence, dU_R/dz is assumed to be constant by Ref. [37].

Ref. [21] is identical to the form of Ref. [37] but assumes time dependency in dU_R/dz by adding an annual component with the following form:

$$\frac{dU_R}{dz}(t) = 0.75 - 2.25\cos\left(\frac{2\pi t}{365}\right), \tag{A11}$$

where t is expressed in day. Ref. [21] illustrates the seasonal variation of the stratospheric circulation by adapting the periodic radiative heating.

Ref. [17] further simplified Refs. [21,37] by using finite differences in just a single layer. They considered $j = 0, 1, 2$ in the finite difference scheme and used variables defined at the middle height $z_T/2$ with $\Delta z = z_T/2$ (z_T is assumed to be 50 km here). Boundary conditions are taken into account at the top and bottom. This produces the approximation:

$$
\begin{aligned}
\frac{\partial \Psi}{\partial z} &= \frac{\Psi_2 - \Psi_0}{2\Delta z} = -\frac{gh}{f_0 z_T}, \\
\frac{\partial^2 \Psi}{\partial z^2} &= \frac{\Psi_2 - 2\Psi_1 + \Psi_0}{\Delta z^2} = -\frac{8\Psi}{z_T^2} + \frac{4gh}{f_0 z_T^2}, \\
\frac{\partial U}{\partial z} &= \frac{U_2 - U_0}{2\Delta z} = \frac{U_1 - U_R(0) + \Lambda z_T/2}{z_T}, \\
\frac{\partial^2 U}{\partial z^2} &= \frac{U_2 - 2U_1 + U_0}{\Delta z^2} = -\frac{4(U_1 - U_R(0) - \Lambda z_T/2)}{z_T^2}.
\end{aligned}
\tag{A12}
$$

This reduction of Yoden's 81 ordinary differential equations removes the vertical dependence. We rewrite $\Psi = X(t) + iY(t)$ and substitute (A12) back into the linearized quasi-geostrophic potential vorticity equation and zonal wind prediction equation. Then, the Ruzmaikin model appears in the final form of three ordinary differential equations:

$$
\begin{aligned}
\dot{X} &= -X/\tau_1 - rY + sUY - \xi\Psi_0 + \delta_w\dot{\Psi}_0, \\
\dot{Y} &= -Y/\tau_1 - rX + sUX + \zeta\Psi_0 U, \\
\dot{U} &= -(U - U_R)/\tau_2 - \eta\Psi_0 Y - \delta_\Lambda\dot{\Lambda},
\end{aligned}
\tag{A13}
$$

where $U_R = U_R(z_T/2) = U_R(0) - \Lambda z_T/2$. The appendix of Ref. [17] gives the derivation of all other fixed parameters, reported in Table A1.

Table A1. Coefficients of the Ruzmaikin model (1)–(3), which are dimensionless unless otherwise noted.

Parameter	Value
τ_1	122.6276
r	0.6286
s	1.9638
ξ	1.7488
δ_w	70.8437
ζ	240.5361
U_R	0.4748
τ_2	30.3713
η	9.131×10^4
δ_Λ	4.9115×10^{-4}
Λ_0	0.75 m/s/km
$\delta\Lambda_a$	2.25 m/s/km
ϵ	0–0.3

Appendix B

This section reviews the mathematical formulation underlying the particle filter. Notation and outline borrowed from Ref. [12]. Then, the functions and variables are defined in the context of the model and data described in Sections 2.1 and 2.2, respectively.

Let $x_k \in \mathbb{R}^n$ be the state vector which evolves according to the system model

$$x_{k+1} = f_k(x_k, w_k) \tag{A14}$$

where $f_k : \mathbb{R}^n \times \mathbb{R}^m \to \mathbb{R}^n$ and $w_k \in \mathbb{R}^m$ is a zero-mean, white-noise sequence independent of x. Let $y_k \in \mathbb{R}^p$ represent observations which are related to x_k through the observation equation

$$y_k = h_k(x_k, v_k) \tag{A15}$$

where $h_k : \mathbb{R}^p \times \mathbb{R}^r \to \mathbb{R}^p$ is the observation operator and $v_k \in \mathbb{R}^r$ is another zero mean, white-noise sequence with known distribution independent of x_k and w_k.

The goal of the particle filter is to construct the density of x_k given all preceding observations $D_k = \{y_i : i = 1, \ldots, k\}$. This is done via recursion and Bayes' rule, which states

$$p(x_k|D_k) = \frac{p(y_k|x_k)p(x_k|D_{k-1})}{p(y_k|D_{k-1})}. \tag{A16}$$

Note that each term in this equation can be written as a function of known variables. Indeed, the denominator is

$$p(y_k|D_{k-1}) = \int p(y_k|x_k)p(x_k|D_{k-1})dx_k \tag{A17}$$

where the first term in the integrand (and numerator of (6)) can be written as

$$p(y_k|x_k) = \int \delta(y_k - h_k(x_k, v_k))p(v_k)dv_k. \tag{A18}$$

The remaining term in the numerator of (6) can be decomposed similarly,

$$p(x_k|D_{k-1}) = \int p(x_k|x_{k-1})p(x_{k-1}|D_{k-1})dx_{k-1} \tag{A19}$$

again writing the first term in the integrand as

$$p(x_k|x_{k-1}) = \int \delta(x_k - f_{k-1}(x_{k-1}, w_{k-1}))p(w_{k-1})dw_{k-1}. \tag{A20}$$

Thus, Bayes' rule can be rewritten in terms of known quantities and the recursively defined $p(x_{k-1}|D_{k-1})$. Analytical solutions to this problem are available for the constrained case for linear f_k, h_k and Gaussian distributions. For more general applications, including the one considered here, the following numerical algorithm is utilized instead.

Consider a set of random samples $\{x_{k-1}(i) : i = 1, \ldots N\}$ of known distribution $p(x_{k-1}|D_{k-1})$. The prediction step involves calculating

$$x_k^*(i) = f_{k-1}(x_{k-1}(i), w_{k-1}(i)) \tag{A21}$$

where $w_{k-1}(i)$ is sampled from the known distribution $p(w_{k-1})$. Clearly, $\{x_k^*(i)\}$ is distributed as $p(x_k|D_{k-1})$.

An update is then preformed by resampling N times with replacement according to the discrete distribution where the weight for the $i-$th ensemble member is given by

$$q_i = \frac{p(y_k|x_k^*(i))}{\sum_{j=1}^N p(y_k|x_k^*(j))}, \tag{A22}$$

to get $\{x_k(i) : i = 1, \ldots, N\}$, which is distributed as $p(x_k|D_k)$ according to Ref. [25].

In the application to stratospheric zonal winds studied here, we have the following particle filter functions and distributions. The state vector is

$$x_k = \begin{pmatrix} X & Y & U & h & \Lambda_0 & \Lambda_a \end{pmatrix}^T, \tag{A23}$$

which evolves according to the dynamical model, f_k, given by numerically solving (using ode4 [45] in MATLAB 2022a) the system of ODEs (1)–(3) and evolving X, Y, and U according to the solution, and adding model error, $w_k \sim N(0, \Sigma_{\text{model}})$. The observed variable is $y_k = U$, related to state vector by the observation equation

$$y_k = x_k^T e_3 + v_k \tag{A24}$$

where $e_3 = \begin{pmatrix} 0 & 0 & 1 & 0 & 0 & 0 \end{pmatrix}^T$, and the observation error is assumed to mean-zero Gaussian noise, $v_k \sim N(0, \sigma_{\text{obs}}^2)$.

The covariance matrix of model error, Σ_{model}, is diagonal with elements set to 0.1% of the maximum values for each state variable X, Y, and U. This was determined by running the Ruzmaikin model with perturbations of varying magnitude between timesteps. Ultimately, we chose the largest variance that allows for some "switching" between high and low stable equilibrium wind speeds without totally disrupting the model. Note that this also agrees fairly well with the method described in Ref. [34], of using the variance-covariance matrix to estimate "natural" variation in a free run to use as an estimate of model variance.

Appendix C

Here, we further explore the ESMDA scheme applied to a parameterized $\Lambda(t)$ as in Equation (17) and a free $h(t) \in \mathbb{R}^N$. In Section 3.2.3, hereafter referred to as "case 1", recall that we were unable to hit the winter peaks using estimated Λ_0, Λ_a, ϵ, and shift parameters. Thus, we try to constrain these parameters to enforce larger values of Λ, so that it may enter the region of bistability.

In Figure A1, we fix the parameters in Equation (17) except for the shift parameters and set them to the values in Ref. [17] (case 2). We do this to enforce a larger amplitude for $\Lambda(t)$ and examine if a time dependent h is enough in this case to produce an analysis consistent with the ECMWF data and the peaks represented in it. We note larger values in RMSE than in case 1 shown in Figure A1a, however the inverse relationship between the RMSE and variance of U in case one is no longer present. In Figure A1b, we can see that for the lowest RMSE results the average value of $h(t)$ is highest, and higher than those in case 1. This results from the larger amplitude of $\Lambda(t)$ being enforced, h will generally need to be higher to drive the resulting higher mean zonal winds down. In Figure A1d we see that we are still unable to capture the peaks despite the larger amplitude of $\Lambda(t)$ evidenced in Figure A1e. In addition, the troughs are overshot, likely resulting from the large values of h required to bring down mean zonal wind amplitudes. In Figure A1c we show normalized $\Lambda(t)$, $U(t)$, and $h(t)$ for the case where $\tau_h = 91$, again corresponding to the lowest RMSE for mean zonal wind.
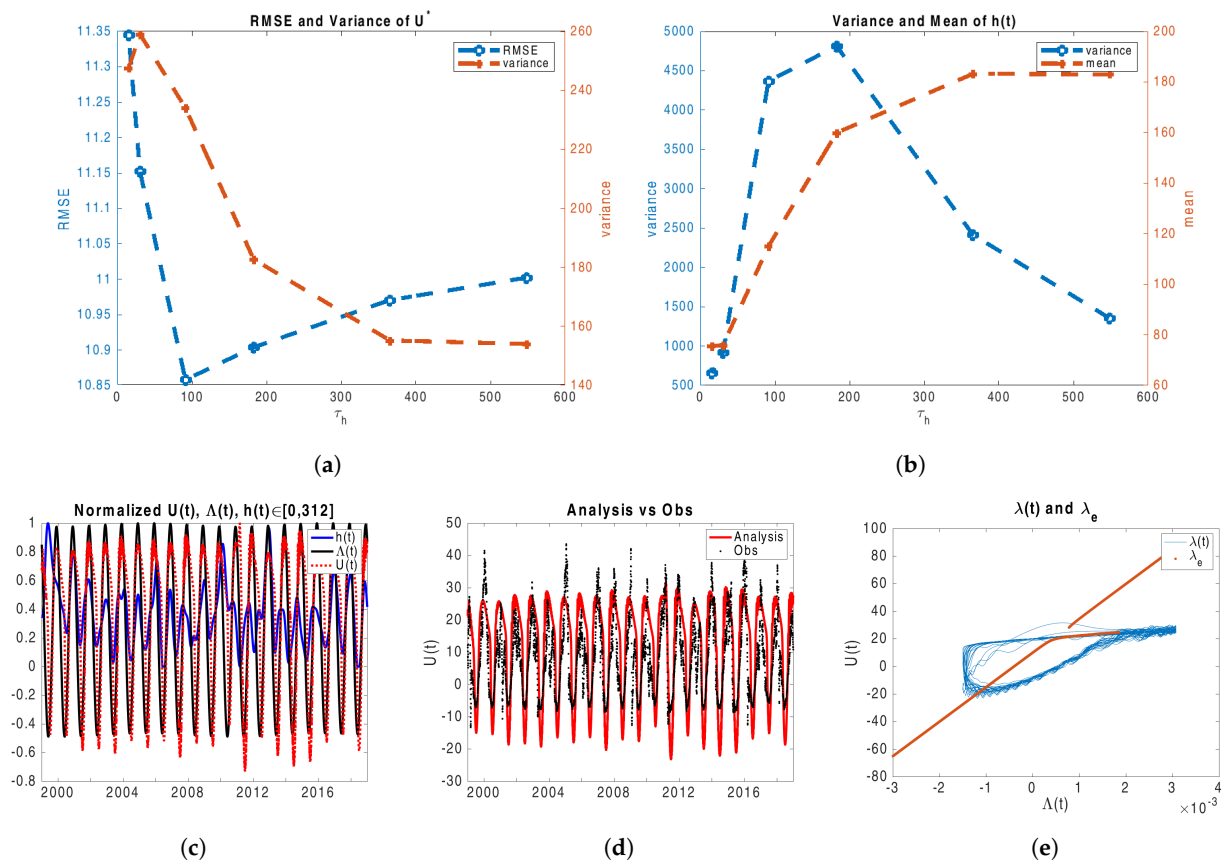
Figure A1. Results from ESMDA fraternal twin experiments for $\Lambda(t)$ parameterized by $\Lambda_0 = 0.75$, $\Lambda_a = 2.25$ m/s/km, and $\epsilon = 0.3$ fixed and $h(t)$ free. (**a**) RMSE (blue) and variance (orange) of model analysis $U(t)$ while (**b**) shows the variance (blue) and mean (orange) of $h(t)$, each for varying values of τ_h. (**c**) Model output for variables normalized U (red), h (blue), and Λ (black). (**d**) Comparison of model estimated wind speeds (red) with the observed wind speeds (black). (**e**) $\Lambda - U$ phase space of model output (blue) superimposed on the bifurcation diagram for Λ (orange). (**c–e**) Model output is from the lowest RMSE experiment ($\tau_h = 91$).

Finally, using the results shown in Figure A2 we again use the ESMDA scheme to estimate Λ_0, Λ_a, and ϵ, as well as the shift parameters, but provide a minimum value for Λ_a to be that set in Ref. [17]. This is done to sample larger amplitudes in an attempt to find an $h(t)$, which can allow for a close match of the data while capturing the peaks. The results are similar to the previous case with the lowest RMSE occurring for $\tau_h = 547$. The estimated amplitudes are indeed larger, which can be seen in Figure A2e, however we are still unable to capture the peaks and the troughs are also overshot as in case 2, shown in Figure A2a. We also see larger average values for $h(t)$, Figure A2b, than cases 1 or 2, owing to the larger amplitudes in $\Lambda(t)$.

(**a**)   (**b**)

(**c**)   (**d**)   (**e**)
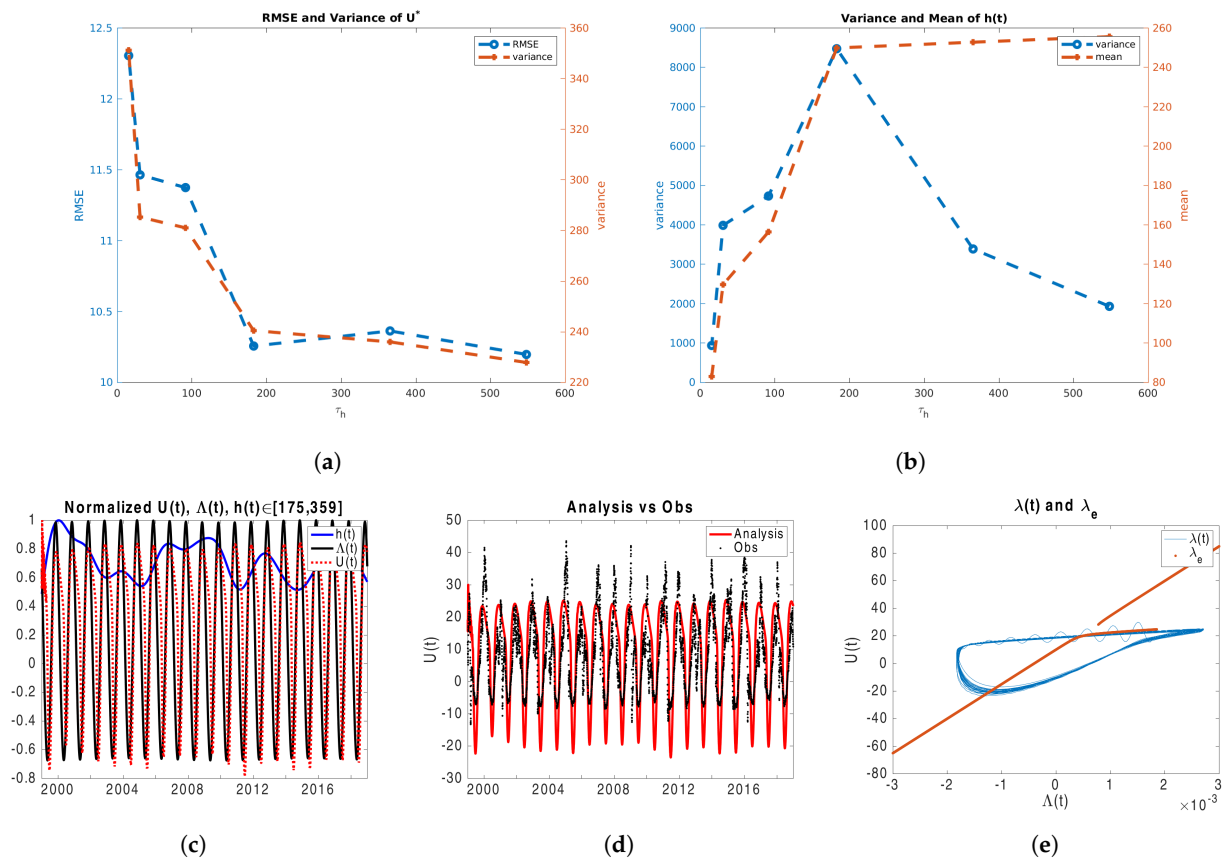
Figure A2. Results from ESMDA fraternal twin experiments with $\Lambda(t)$ parameterized by Λ_0 and ϵ free, $\Lambda_a \geq 2.25$ m/s/km, and $h(t)$ free. (**a**) RMSE (blue) and variance (orange) of model analysis $U(t)$ while (**b**) shows the variance (blue) and mean (orange) of $h(t)$, each for varying values of τ_h. (**c**) Model output for variables normalized U (red), h (blue), and Λ (black). (**d**) Comparison of model estimated wind speeds (red) with the observed wind speeds (black). (**e**) $\Lambda - U$ phase space of model output (blue) superimposed on the bifurcation diagram for Λ (orange). (**c**–**e**) Model output is from the lowest RMSE experiment ($\tau_h = 547$).
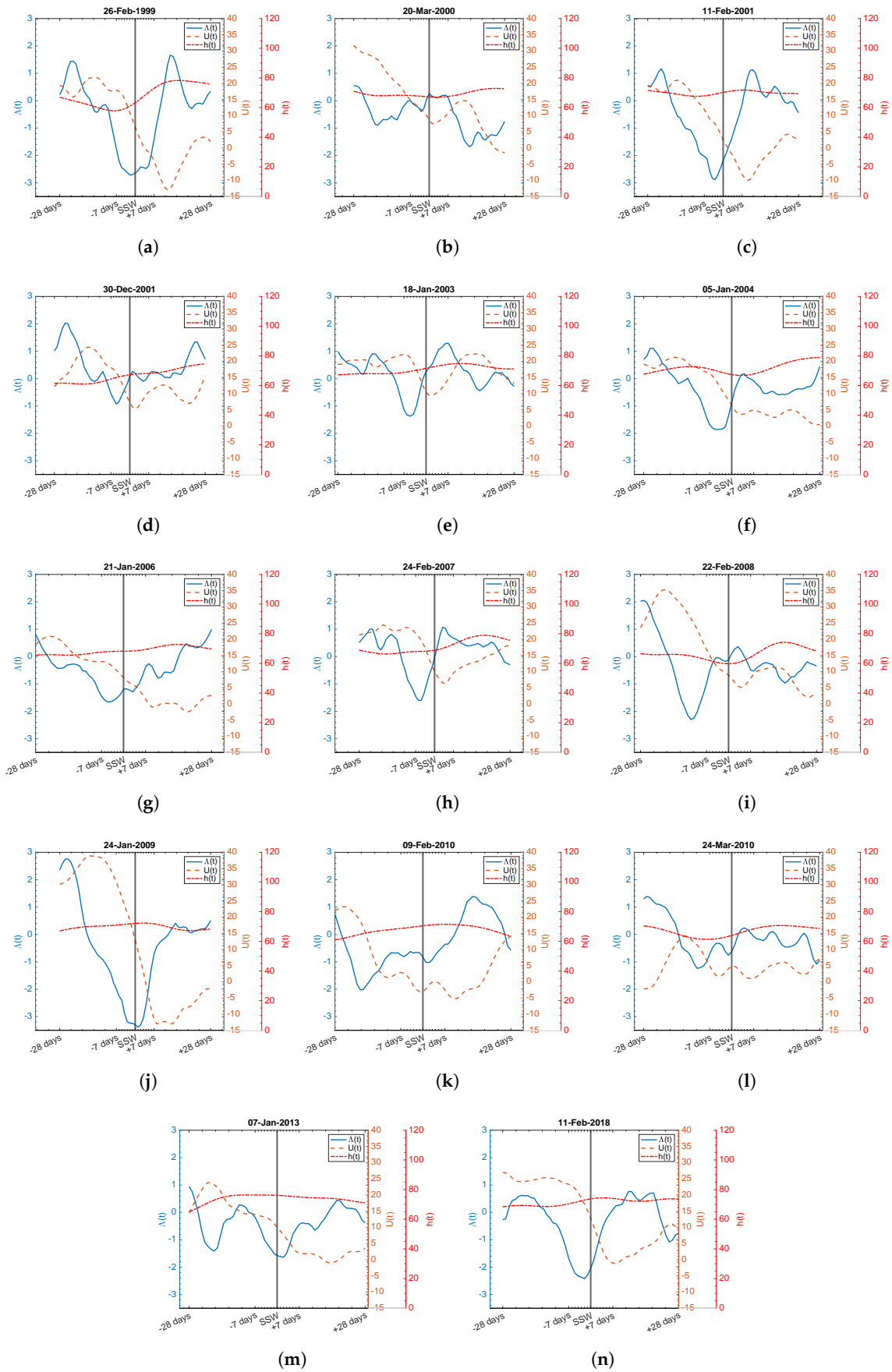
Appendix D

Here, we show the full results of ESMDA analysis behavior around SSW events for varying decorrelation lengths.
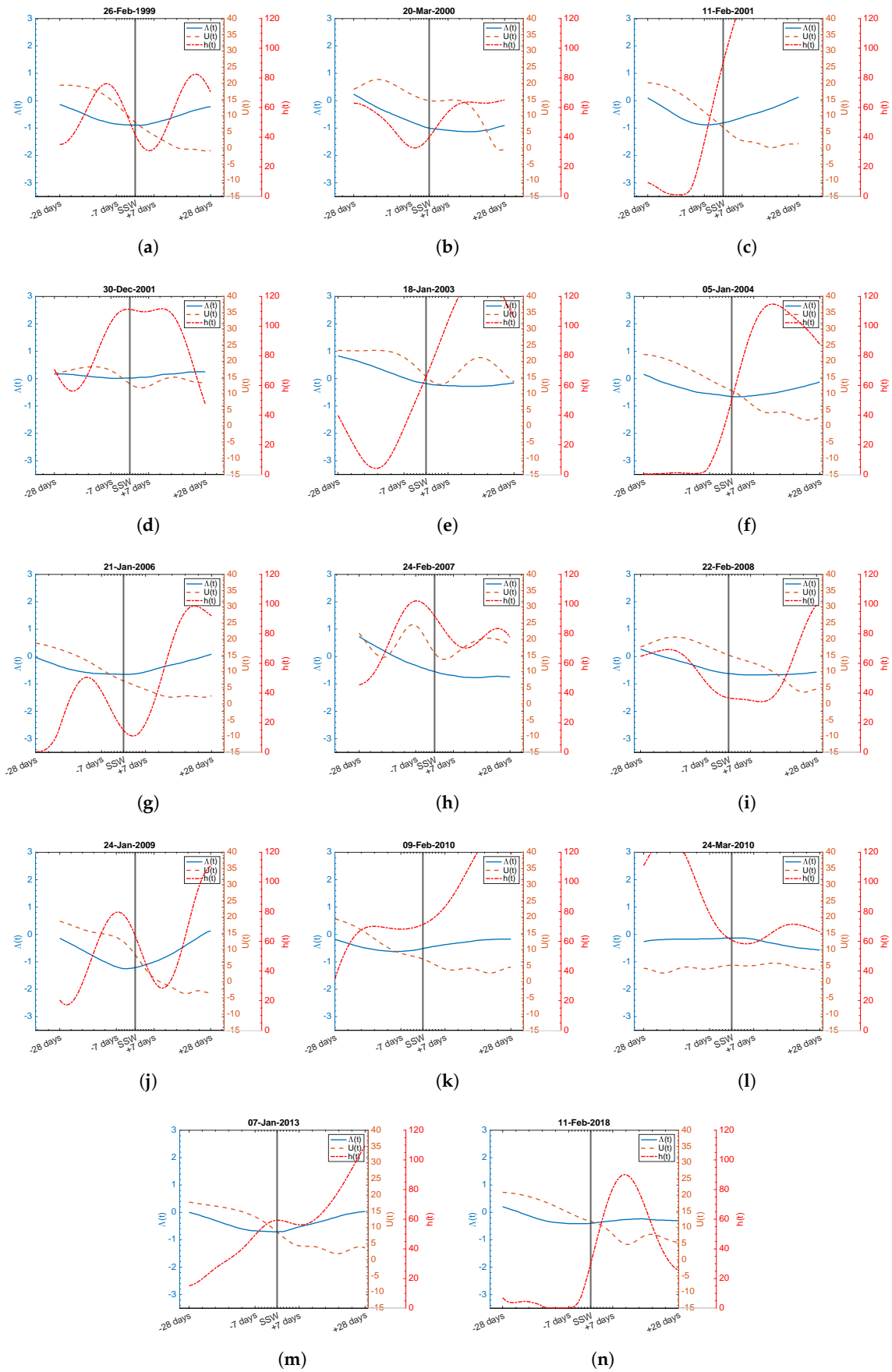
Figure A3. (**a**–**n**) Λ (blue), U (orange), and h (red) around known SSW events with $\tau_\lambda = 547$, $\tau_h = 15$.
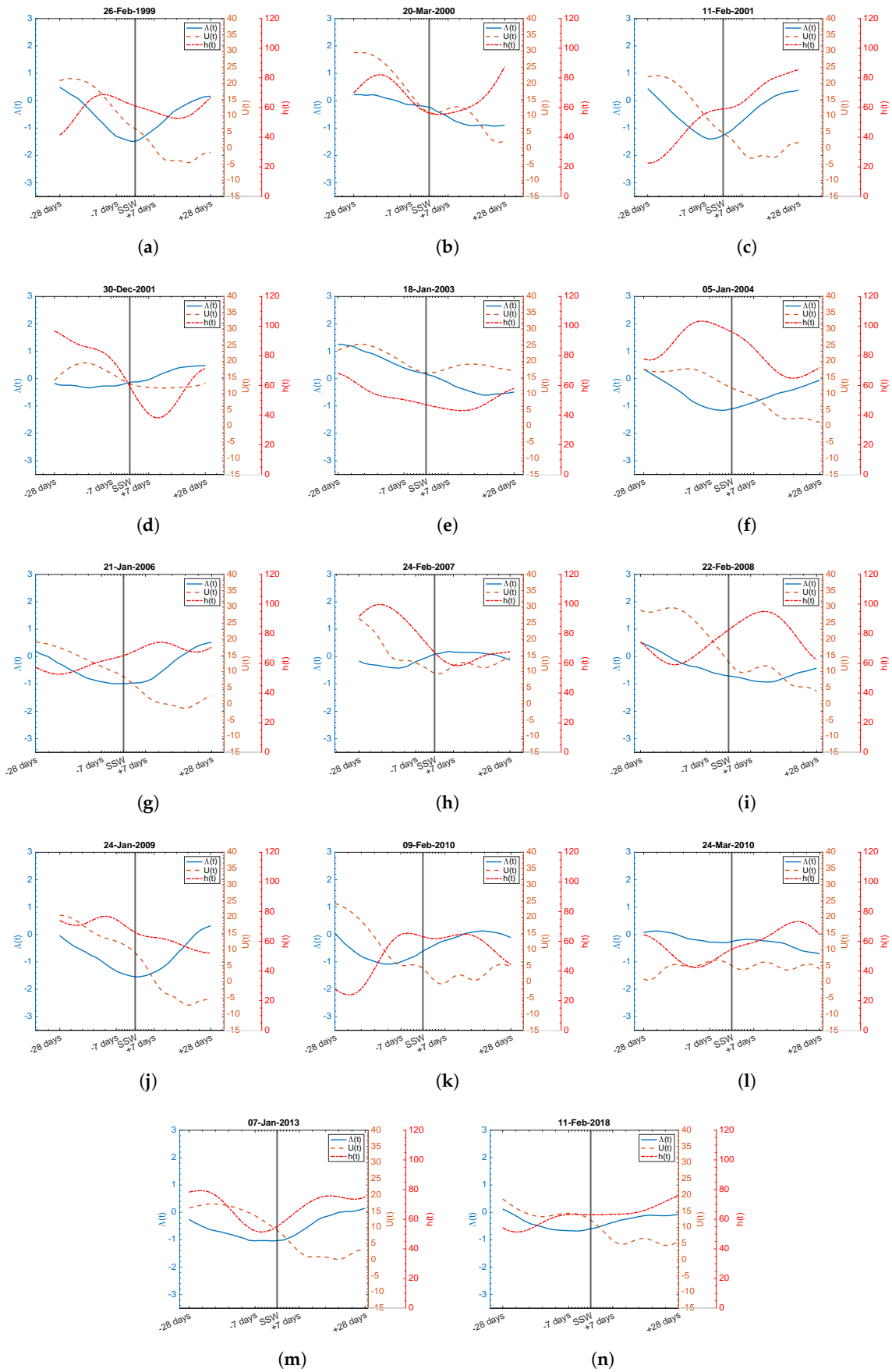
Figure A4. (**a–n**) Λ (blue), U (orange), and h (red) around known SSW events with $\tau_\lambda = 182$, $\tau_h = 15$.

Figure A5. (**a–n**) Λ (blue), U (orange), and h (red) around known SSW events with $\tau_\lambda = 15$, $\tau_h = 15$.

References

1. Muench, H.S. On the dynamics of the wintertime stratosphere circulation. *J. Atmos. Sci.* **1965**, *22*, 349–360. [CrossRef]
2. Geisler, J. A numerical model of the sudden stratospheric warming mechanism. *J. Geophys. Res.* **1974**, *79*, 4989–4999. [CrossRef]
3. Charney, J.G.; DeVore, J.G. Multiple flow equilibria in the atmosphere and blocking. *J. Atmos. Sci.* **1979**, *36*, 1205–1216. [CrossRef]
4. Ambaum, M.H.P.; Hoskins, B.J. The NAO Troposphere–Stratosphere Connection. *J. Clim.* **2002**, *15*, 1969–1978. [CrossRef]
5. Finkel, J.; Abbot, D.S.; Weare, J. Path properties of atmospheric transitions: Illustration with a low-order sudden stratospheric warming model. *J. Atmos. Sci.* **2020**, *77*, 2327–2347. [CrossRef]
6. Holton, J.R.; Mass, C. Stratospheric vacillation cycles. *J. Atmos. Sci.* **1976**, *33*, 2218–2225. [CrossRef]
7. McIntyre, M.E. How well do we understand the dynamics of stratospheric warmings? *J. Meteorol. Soc. Japan. Ser. II* **1982**, *60*, 37–65. [CrossRef]
8. Scott, R.; Polvani, L.M. Internal variability of the winter stratosphere. Part I: Time-independent forcing. *J. Atmos. Sci.* **2006**, *63*, 2758–2776. [CrossRef]
9. Stan, C.; Straus, D.M. Stratospheric predictability and sudden stratospheric warming events. *J. Geophys. Res. Atmos.* **2009**, *114*. [CrossRef]
10. Jeppesen, J. Fact Sheet: Reanalysis. 2020. Available online: https://www.ecmwf.int/en/about/media-centre/focus/2020/fact-sheet-reanalysis (accessed on 31 July 2021).
11. Kantas, N.; Doucet, A.; Singh, S.S.; Maciejowski, J.; Chopin, N. On particle methods for parameter estimation in state-space models. *Stat. Sci.* **2015**, *30*, 328–351. [CrossRef]
12. Gordon, N.J.; Salmond, D.J.; Smith, A.F. Novel approach to nonlinear/non-Gaussian Bayesian state estimation. In *Proceedings of the IEE Proceedings F-Radar and Signal Processing*; IET: Stevenage, UK, 1993; Volume 140, pp. 107–113.
13. Asch, M.; Bocquet, M.; Nodet, M. *Data Assimilation: Methods, Algorithms, and Applications*; SIAM, Society for Industrial and Applied Mathematics: Philadelphia, PA, USA, 2016.
14. Bocquet, M.; Sakov, P. An iterative ensemble Kalman smoother. *Q. J. R. Meteorol. Soc.* **2013**, *140*, 1521–1535. [CrossRef]
15. Carrassi, A.; Bocquet, M.; Bertino, L.; Evensen, G. Data Assimilation in the Geosciences—An overview on methods, issues and perspectives. *arXiv* **2018**, arXiv:1709.02798.
16. Skjervheim, J.; Evensen, G. An ensemble smoother for assisted history matching. In Proceedings of the SPE Reservoir Simulation Symposium, Woodlands, TX, USA, 21–23 February 2011; SPE 141929; SPE: Richardson, TX, USA, 2011. [CrossRef]
17. Ruzmaikin, A.; Lawrence, J.; Cadavid, C. A simple model of stratospheric dynamics including solar variability. *J. Clim.* **2003**, *16*, 1593–1600. [CrossRef]
18. Andrews, D.G.; Holton, J.R.; Leovy, C.B. *Middle Atmosphere Dynamics*; Number 40; Academic Press: Cambridge, MA, USA, 1987.
19. Eichelberger, S.J.; Holton, J.R. A mechanistic model of the northern annular mode. *J. Geophys. Res. Atmos.* **2002**, *107*, ACL 10-1–ACL 10-12. [CrossRef]
20. Wakata, Y.; Uryu, M. Stratospheric multiple equilibria and seasonal variations. *J. Meteorol. Soc. Japan. Ser. II* **1987**, *65*, 27–42. [CrossRef]
21. Yoden, S. An illustrative model of seasonal and interannual variations of the stratospheric circulation. *J. Atmos. Sci.* **1990**, *47*, 1845–1853. [CrossRef]
22. Sanchez, K. Understanding the Stratospheric Polar Vortex: A Parameter Sensitivity Analysis on a Simple Model of Stratospheric Dynamics. Ph.D. Thesis, Sam Houston State University, Huntsville, TX, USA, 2020.
23. Berrisford, P.; Kållberg, P.; Kobayashi, S.; Dee, D.; Uppala, S.; Simmons, A.; Poli, P.; Sato, H. Atmospheric conservation properties in ERA-Interim. *Q. J. R. Meteorol. Soc.* **2011**, *137*, 1381–1399. [CrossRef]
24. Wu, Z. Data Assimilation and Uncertainty Quantification with Reduced-order Models. Ph.D. Thesis, Arizona State University, Tempe, AZ, USA, 2021.
25. Smith, A.F.; Gelfand, A.E. Bayesian statistics without tears: A sampling–resampling perspective. *Am. Stat.* **1992**, *46*, 84–88.
26. Marín, D.A.A. Particle Filter Tutorial. 2012. Available online: https://www.mathworks.com/matlabcentral/fileexchange/35468-particle-filter-tutorial (accessed on 2 April 2021).
27. Pfister, R.; Schwarz, K.A.; Janczyk, M.; Dale, R.; Freeman, J. Good things peak in pairs: A note on the bimodality coefficient. *Front. Psychol.* **2013**, *4*, 700. [CrossRef]
28. Freeman, J.B.; Dale, R. Assessing bimodality to detect the presence of a dual cognitive process. *Behav. Res. Methods* **2013**, *45*, 83–97. [CrossRef]
29. Emerick, A.A.; Reynolds, A.C. Ensemble smoother with multiple data assimilation. *Comput. Geosci.* **2013**, *55*, 3–15. [CrossRef]
30. Fleurantin, E.; Sampson, C.; Maes, D.P.; Bennett, J.; Fernandes-Nunez, T.; Marx, S.; Evensen, G. A study of disproportionately affected populations by race/ethnicity during the SARS-CoV-2 pandemic using multi-population SEIR modeling and ensemble data assimilation. *Found. Data Sci.* **2021**, *3*, 479–541. [CrossRef]
31. Evensen, G. EnKF_seir. 2021. Available online: https://github.com/geirev/EnKF_seir (accessed on 30 January 2021)
32. Lawson, L.M.; Spitz, Y.H.; Hofmann, E.E.; Long, R.B. A data assimilation technique applied to a predator-prey model. *Bull. Math. Biol.* **1995**, *57*, 593–617. [CrossRef]
33. Houtekamer, P.L.; Mitchell, H.L. Data assimilation using an ensemble Kalman filter technique. *Mon. Weather Rev.* **1998**, *126*, 796–811. [CrossRef]

34. Browne, P.; Van Leeuwen, P. Twin experiments with the equivalent weights particle filter and HadCM3. *Q. J. R. Meteorol. Soc.* **2015**, *141*, 3399–3414. [CrossRef]

35. Evensen, G. The Ensemble Kalman Filter: Theoretical formulation and practical implementation. *Ocean Dyn.* **2003**, *53*, 343–367. [CrossRef]

36. Evensen, G. Sampling strategies and square root analysis schemes for the EnKF. *Ocean Dyn.* **2004**, *54*, 539–560. [CrossRef]

37. Yoden, S. Bifurcation properties of a stratospheric vacillation model. *J. Atmos. Sci.* **1987**, *44*, 1723–1733. [CrossRef]

38. Butler, A.H. *Table of Major Mid-Winter SSWs in Reanalyses Products*; NOAA Chemical Science Laboratory: Boulder, CO, USA, 2020. Available online: https://csl.noaa.gov/groups/csl8/sswcompendium/majorevents.html (accessed on 6 July 2023).

39. Butler, A.H.; Seidel, D.J.; Hardiman, S.C.; Butchart, N.; Birner, T.; Match, A. Defining Sudden Stratospheric Warmings. *Bull. Am. Meteorol. Soc.* **2015**, *96*, 1913–1928. [CrossRef]

40. Charlton, A.J.; Polvani, L.M. A New Look at Stratospheric Sudden Warmings. Part I: Climatology and Modeling Benchmarks. *J. Clim.* **2007**, *20*, 449–469. [CrossRef]

41. Zuev, V.V.; Savelieva, E. Arctic polar vortex dynamics during winter 2006/2007. *Polar Sci.* **2020**, *25*, 100532. [CrossRef]

42. Manabe, S.; Wetherald, R.T. Thermal Equilibrium of the Atmosphere with a Given Distribution of Relative Humidity. *J. Atmos. Sci.* **1967**, *24*, 241–259. [CrossRef]

43. Santer, B.D.; Po-Chedley, S.; Zhao, L.; Zou, C.Z.; Fu, Q.; Solomon, S.; Thompson, D.W.J.; Mears, C.; Taylor, K.E. Exceptional stratospheric contribution to human fingerprints on atmospheric temperature. *Proc. Natl. Acad. Sci. USA* **2023**, *120*, e2300758120. [CrossRef]

44. Holton, J.R.; Dunkerton, T. On the role of wave transience and dissipation in stratospheric mean flow vacillations. *J. Atmos. Sci.* **1978**, *35*, 740–744. [CrossRef]

45. Keevil, J. ODE4 Gives More Accurate Results than ODE45, ODE23, ODE23s. 2016. Available online: https://www.mathworks.com/matlabcentral/fileexchange/59044-ode4-gives-more-accurate-results-than-ode45-ode23-ode23s (accessed on 13 May 2021).